

1 **Crustal velocity variations and constraints on material**
2 **properties in the Charlevoix Seismic Zone, eastern**
3 **Canada**

4 **J. Onwuemeka^{1*}, Y. Liu¹, and R. M. Harrington²**

5 ¹Department of Earth and Planetary Sciences, McGill University, Montreal, Quebec, Canada

6 ²Institute of Geology, Mineralogy, and Geophysics, Ruhr University, Bochum, Germany

7 **Key Points:**

- 8 • Lower velocities and a diffuse earthquake distribution are prevalent inside the
9 Charlevoix impact structure due to intense fracturing
- 10 • Porosity enhancement of up to 10% by low (0.1) aspect ratio cracks explain
11 velocity variations inside the impact structure
- 12 • Compositional alteration dominates crustal seismic velocities outside the
13 impact structure

*Current address: Dept. of Earth and Planetary Sciences, McGill University, Montreal, Quebec, Canada

Corresponding author: John Onwuemeka, john.onwuemeka@mail.mcgill.ca

14 Abstract

15 Crustal velocity variation within impact-related seismic zones is commonly
16 attributed to mechanisms such as pore pressure changes, dense fracture network, and
17 compositional variation. In this study, we combine seismic tomography, rock physics
18 analysis, and potential field modeling to quantitatively investigate the mechanisms
19 that influence crustal velocity variation in the Charlevoix Seismic Zone (CSZ), a
20 meteorite impact-related seismic zone in eastern Canada. Earthquakes in the CSZ
21 align along two broad NE-SW trending clusters related to reactivated paleo-rift
22 faults. Within the impact structure, the earthquakes are diffusely distributed and
23 lower velocity bodies are ubiquitous which can be attributed to crustal damage from
24 tectonic inheritance exacerbated by the meteorite impact. The Bouguer gravity
25 anomaly decreases southeastward across the St. Lawrence River due to density
26 disparity between rocks in the Grenville Province and the Appalachians. We find a
27 higher velocity body northeast of the impact structure that does not exhibit an
28 observable gravity anomaly, which suggests the presence of a rock (e.g. anorthosite)
29 of comparable density but a higher elastic moduli within another rock (e.g.
30 charnockite). Outside the impact structure, compositional variations control velocity
31 changes, whereas inside the impact structure, velocity variations can be explained by
32 porosity enhancement of up to 10% by low (0.1) aspect ratio cracks. Our results
33 suggest that intense fracturing and compositional alteration, rather than pore
34 pressure, control velocity variations, hence earthquake processes in the CSZ.

35 1. Introduction

36 Intraplate seismicity occurs in stable plate interiors away from tectonic plate
37 boundaries. The typical strain rates ($\leq 10^{-10} \text{ yr}^{-1}$) within intraplate seismic zones
38 are 2 or more orders of magnitude less than average strain rates ($\geq 10^{-8} \text{ yr}^{-1}$)
39 reported for seismogenic plate boundary faults (e.g., Gordon, 1998; Mazzotti &
40 Adams, 2005; Mazzotti & Gueydan, 2018). Consequently, seismogenic faults in
41 intraplate seismic zones produce moderate-to-large earthquakes (e.g., 2001 **M** 7 Bhuj
42 earthquake, 1811-1812 \sim **M** 7 New Madrid earthquakes) less frequently than their
43 plate boundary analogues (Hough et al., 2004; Bendick et al., 2001), but their
44 physical mechanisms remain poorly understood. Steady tectonic loading in plate
45 interiors could be attributed to basal traction, gravitational body forces, and plate

46 boundary forces (Liu & Stein, 2016). However, these mechanisms are not always
47 sufficient to elevate stresses to levels that trigger failure on intraplate faults, and are
48 unlikely to be entirely responsible for the stress budget within intraplate seismic
49 zones. Several studies show that earthquakes within plate interiors concentrate
50 within zones of inherited crustal weaknesses due to factors such as, tectonics,
51 volcanism, and meteorite impacts (e.g., Bendick et al., 2001; Mazzotti & Gueydan,
52 2018; Sykes, 1978; Tarayoun et al., 2018). Therefore, mechanisms such as postglacial
53 rebound, loading from distal plate boundaries, and localized lithospheric-scale
54 structural weaknesses (i.e., stress amplifiers) due to prior tectonic episodes are
55 collectively invoked to explain loading on seismogenic faults within intraplate seismic
56 zones (Liu & Stein, 2016; Mazzotti & Gueydan, 2018). The structural weaknesses
57 potentially link to dense fracture networks and density disparities. In order to better
58 understand processes and mechanisms that control earthquake processes within
59 intraplate seismic zones, it is important to investigate the distribution of tectonic
60 structures such as faults, fracture zones, and material compositions due to their
61 primary effect on crustal stresses. Such investigation is paramount to constrain
62 physical mechanisms that control seismicity, especially for complex intraplate seismic
63 zones such as the Charlevoix Seismic Zone (CSZ) in eastern Canada.

64 The CSZ is located in Quebec along the St. Lawrence paleo-rift system within the
65 stable North American continental interior. It has been recognized as the most
66 active seismic zone in eastern Canada (Fig. 1). Present-day geological features of
67 the CSZ derive from previous significant tectonic episodes, including Grenville
68 orogeny, opening of the Iapetus ocean, and Taconian orogeny, that created a weak
69 zone which was overprinted by a late Ordovician to early Silurian meteorite impact
70 (Rondot, 1971; Lemieux et al., 2003; Schmieder et al., 2019). The meteorite impact
71 structure crosscuts pre-existing NE-SW trending normal faults of the St. Lawrence
72 rift system. Major rifts within the CSZ, including Charlevoix, Gouffre River, and St.
73 Lawrence faults, have been found to dominate distribution of seismicity in the CSZ
74 (Onwuemeka et al., 2018; Powell & Lamontagne, 2017; Yu et al., 2016). Mesozoic
75 reverse-sense fault reactivation due to ridge-push force following the opening of
76 Atlantic Ocean is thought to contribute to the current stress perturbation
77 responsible for the seismicity in the CSZ (Lemieux et al., 2003; Ma & Eaton, 2007).
78 In addition, glacial unloading following the Wisconsin glaciation (85 - 11 kyr) is

79 interpreted to exert post-glacial rebound stress on critically stressed faults in the
80 pre-weakened structural zones (Wu & Hasegawa, 1996; Tarayoun et al., 2018).
81 Historically, five $M 6+$ earthquakes occurred in the CSZ since 1663, with at least
82 another two $M 6+$ in the past 10,000 years prior to the 1663 event based on
83 paleo-seismic studies (Tuttle & Atkinson, 2010). The evidence of $M 6+$ events is
84 seen in liquefaction features (e.g., basal erosion, sand dikes, and diapirs) that are
85 typical of strong ground-shaking and fault rocks such as pseudotachylytes formed as
86 a result of shear-related frictional melting (Lemieux et al., 2003). Previous studies
87 (e.g., Onwuemeka et al., 2018; Yu et al., 2016) found that earthquakes in the CSZ
88 are diffusely distributed within the impact structure, nevertheless, they broadly
89 define two NE-SW trending clusters that highlight the high (up to 60°) dip angle of
90 the reactivated Iapetan normal faults.

91 The unique, but complex, tectonic setting of the CSZ necessitates adequate
92 assessment to quantify the contributions of the different physical mechanisms such
93 as intense fracturing and compositional variation to its current velocity structure,
94 and to relate the velocity structures to earthquake processes. Previous studies (e.g.,
95 Baird et al., 2010; Mazzotti, 2007; Mazzotti & Gueydan, 2018; Fadugba et al., 2019)
96 suggest that tectonic inheritance (e.g., diffusely distributed fracture networks) acts
97 to locally concentrate stress and potentially control the distribution of earthquakes.
98 Variations in rock composition could similarly enhance local stresses due to lateral
99 imbalance of gravitational potential energy caused by intramural density and shear
100 strength disparity (Liu & Stein, 2016). Compositional variation has been suggested
101 as a contributing factor to stress concentration in the Western Quebec seismic zone
102 which is located southwest of the CSZ within the St. Lawrence rift system (e.g.,
103 Dineva et al., 2007). Thus, the objective of this work is to quantify the spatial
104 extent and relative contributions of (1) intense fracturing, and (2) compositional
105 variation on velocity variations and their control on earthquake processes in the
106 CSZ.

107 Passive source seismic tomography has been used extensively to study the Earth's
108 internal structure at different scales (e.g., Christensen & Mooney, 1995; Ebel et al.,
109 2000; Koulakov et al., 2007, 2009b). Previous tomographic studies in the CSZ (e.g.,
110 Vlahovic et al., 2003; Powell & Lamontagne, 2017) imaged heterogeneous crustal
111 velocities that likely represent the distribution of structural features. Vlahovic et al.

112 (2003) used 3093 P-wave arrival travel-times from 489 earthquakes to perform
113 tomographic inversion and found a dearth of earthquakes near and within
114 high-velocity bodies. Furthermore, the authors found that larger ($M_N \geq 4$) events
115 preferably occur around the edges of high-velocity bodies, particularly at mid-crustal
116 depth around the northeastern edge of the outer rim of the impact structure
117 (Fig. 1). The authors imaged lower velocities at mid-crustal depths at the center of
118 the impact structure surrounded by higher velocity bodies (Fig. 9 in Vlahovic et al.,
119 2003). They interpret the higher velocity bodies as stronger crust surrounding less
120 competent crust (i.e., the lower velocity bodies). Whereas crustal velocity variations
121 can be inferred with seismic tomography, the results are non-unique therefore would
122 be insufficient to quantify the contributions of any specific mechanism nor more
123 accurately interpret the physical conditions of the crust. Powell and Lamontagne
124 (2017) identified varying velocities across the entire upper to middle crust within the
125 CSZ and suggested that both compositional variation and intense fracturing could
126 be responsible for observed velocity variations. But, the relative contribution of
127 these mechanisms is not yet quantitatively determined.

128 Rock physics analysis and potential field modeling are also powerful tools that can
129 be used to constrain velocity variations and quantify individual contributions from
130 the proposed physical mechanisms. The elastic modulus of a rock is influenced by its
131 material composition as well as its mechanical properties (e.g. internal cracks). For
132 example, an intact rock would have different elastic moduli when compared with a
133 fractured rock of exactly the same material composition. Similarly, a
134 compositionally altered, mechanically intact rock would have different elastic moduli
135 relative to the unaltered state. Therefore, rock physics analysis can be used to
136 quantify the influence of rock properties such as crack volume, crack aspect ratio,
137 and density on the speed of seismic wave propagating through the rock, while
138 potential field modeling (e.g., Bouguer anomaly modeling) can be used to
139 discriminate density disparities. When combined, they can distinguish velocity
140 changes due to compositional variation and intense fracturing. For example,
141 contrasting velocity within an area that does not show observable Bouguer gravity
142 anomaly disparity is mostly likely caused by conglomeration of rocks of differing
143 elastic moduli but similar density. Roland et al. (2012) used rock physics analysis
144 and gravity anomaly modeling to constrain seismic velocity variation at the

145 Quebreda-Discovery-Gofar transform faults, East Pacific Rise. In their study, they
146 found that low-velocity zones at Gofar and Quebreda faults are explained if the
147 porosity is enhanced by up to 8%, and ruled out material alteration such as
148 serpentinization as a contributing mechanism.

149 In this study, we show the results of multi-faceted approach, including tomographic
150 inversion, effective media analysis, and gravity modeling, to quantify the
151 contributions of intense fracturing and rock composition to variations in crustal
152 velocity and seismic behavior in the CSZ. We use local earthquake travel-time
153 tomography (LET) techniques to image velocity structures. We also analyze changes
154 to seismic wave velocity due to material properties (i.e., effective media analysis)
155 and use gravity modeling to constrain the spatial dominance of the material
156 property variation. The effective media analysis incorporates two crustal models, (1)
157 fractured crust, and (2) compositionally altered crust (i.e. crust composed of
158 heterogeneous materials), to derive 3D density models from the observed velocity
159 model. We use the 3D density model to predict Bouguer gravity anomalies and
160 compare the predictions to observations to constrain the mechanism(s) responsible
161 for the velocity changes.

162 **2. 3D velocity structure imaging**

163 **2.1. Seismograph data**

164 Depending on the type of data, tomographic inversion can be used to image
165 structures within a seismic zone to provide insight into structural features that
166 control the earthquake distribution. In this study, we use P- and S-wave first arrival
167 time picks of 2405 local earthquakes (M_N -0.6 - 5.4; M_N is Nuttli magnitude; Nuttli,
168 1973) reported in the Natural Resources Canada (NRCan;
169 <https://earthquakescanada.nrcan.gc.ca/stndon/NEDB-BNDS/bulletin-en.php>
170 last accessed August 2019) earthquake catalog (Jun. 1988 - Mar. 2019 including
171 relocated seismicity of Onwuemeka et al., 2018) for the CSZ to invert for V_p and V_s
172 (Fig. 1). The arrival times are recorded by fourteen CNSN stations (in operation at
173 different times since the 1980s; 7 stations in operation since October, 1994), five
174 Quebec-Maine Transect campaign stations (August 2012 to August 2016), three
175 USArray Transportable Array stations (August 2003 to September 2015), and four

176 temporary campaign stations deployed by McGill University (since July 2015;
 177 Fig. 2). The (automatically picked) phase arrival times of 1626 events reported up
 178 until May, 2012, were retrieved from Yu et al. (2016). The P- and S-wave first
 179 arrival times of the remaining 779 events are manual picks. A total of 17518 catalog
 180 travel-times (8785 for P-wave and 8733 for S-wave) were computed and used as
 181 input for the tomographic inversion. We use the St. Lawrence River south shore
 182 velocity model (Fig. S1) of (Lamontagne, 1999) as the starting 1D velocity model, as
 183 it yields lower travel-time residuals compared with the north shore model
 184 (Onwuemeka et al., 2018).

185 2.2. Travel-time tomography method

186 Travel-time tomography uses a set of known variables (e.g., phase travel-times) and
 187 *a priori* information (e.g., an initial/starting velocity model) to infer model
 188 parameters such as earthquake locations and velocity structure. The synthetic
 189 source-to-station travel-time for each source-station pair is computed based on ray
 190 theory (e.g., Zhang & Thurber, 2003). The travel-time, t_i , from source to station is
 191 given by:

$$192 \quad t_i = \int_{S_i} \frac{ds}{c} \quad (1)$$

193 where c is the velocity model and S_i is the i th ray path. The ray path yielding the
 194 lowest residuals is accepted as the best solution.

195 A 3D ray coverage computed with a ray-tracing algorithm and checkerboard test
 196 provide a quantitative measure of the resolution of a given data set. To avoid bias
 197 by *a priori* information in the checkerboard resolution test, the theoretical
 198 computation of travel-time in the forward problem and inverse problem should be
 199 solved with different algorithms. Here, we use the double-difference travel-time
 200 tomography algorithm, *TomoDD*, (Zhang & Thurber, 2003) a program that
 201 computes ray paths and minimizes residuals with a pseudo-bending ray-tracing
 202 algorithm (Um & Thurber, 1987), to calculate synthetic travel-times within a
 203 checkerboard volume. For the inverse problem, we use the segmented bending
 204 ray-tracing algorithm in *LOTOS* (Koulakov, 2009a). Each individual wave ray path
 205 starts as a straight line from the source location to the observation point and it is
 206 then iteratively deflected in 3D for travel time minimization (Koulakov, 2009a). The

207 ray path with the lowest travel-time residual is selected. *LOTOS* simultaneously
 208 inverts for source coordinates and velocity, and has the option to optimize the input
 209 1D velocity model with the *VELEST* algorithm of Kissling et al. (1994). *LOTOS*
 210 reduces computation time relative to *TomoDD* by defining the velocity
 211 parameterization for nodes, cells, polygons, or any other parameterization. The
 212 inversion grid nodes are adaptive, and nodes without crossing-raypaths are removed
 213 to improve computation efficiency. We refer the readers to Koulakov (2009a) and
 214 references therein for more information regarding *LOTOS*.

215 **2.3. Tomographic inversion algorithm evaluation and parameter setting**

216 **2.3.1 Checkerboard test and tomographic model setup**

217 To test model reliability, we explore wide range of possible parameters that might
 218 affect the tomographic inversion results, including the forward solver, starting
 219 velocity model, source-station geometry, grid size, and noise. A commonly used
 220 technique for resolution analysis is the checkerboard test, which involves creating an
 221 artificial polygons of alternating velocities and simulating seismic sources within the
 222 checkered volume. To better reproduce the uncertainties in real data, we use
 223 *tomoDD* to generate the synthetic travel-times and then add 5% Gaussian noise to
 224 the travel-times to replicate noise. We generate the synthetics with alternating
 225 $\pm 10\%$ perturbations of the 1D south shore velocity model of Lamontagne (1999)
 226 within a 3D volume with checkerboard sizes of 10 km, 6 km, 5 km, and 4 km. We
 227 then invert the synthetic travel-times with *LOTOS*.

228 To further ensure that our synthetic travel-times have similar features common to
 229 real data and the source locations are not constrained *a priori*, we set the source
 230 epicenters to the center of our study area (latitude = 47.53, Longitude = -70.17)
 231 with depths set to 1 km, 5 km, and 10 km for different test runs. Furthermore, we
 232 use different grid node spacing (0.5, 1, and 2 km in all (x,y,z) directions) and choose
 233 the node spacing with the lowest absolute root mean square (RMS) residual as the
 234 optimum spacing for our study. Similarly, we perform a suite of inversion runs with
 235 the damping factor (D) in the range of [0, 0.3] for both P and S waves, and the
 236 smoothing factor (S) of [0.2, 0.6] for P and [0.4, 0.9] for S-waves. The optimal set of
 237 D and S are chosen as those resulting in the lowest RMS residuals, that is, [D, S] =

238 [0, 0.3] for P-waves and [0.3, 0.6] for S-waves. In addition, we use three different 1D
 239 starting velocity models that comprise (1) the 1D south shore, (2) a quasi
 240 layer-over-halfspace, and (3) perturbed 1D velocity models (Fig. S1). The perturbed
 241 1D model is determined by randomized perturbation of V_p , V_s , and depth of the 1D
 242 south shore model with the random number generator function in *Python*[®]. We
 243 note that *LOTOS* internally accounts for the effect of grid node orientation by
 244 stacking velocities computed for 4 different grid orientations (0° , 22° , 45° , and 67°
 245 azimuths). The number of LSQR iterations for each grid orientation of the joint
 246 inversion is 200 in all resolution tests.

247 The inversion setup for the real data is similar to the setup for the resolution
 248 (checkerboard) tests. The optimum smoothing and damping factors are determined
 249 from the resolution analysis. Grid node spacing of 1 km in x, y, and z directions is
 250 preferred as it yields lower RMS and grid orientations are set to 0° , 22° , 45° and
 251 67° , as in the resolution tests. We first optimize the input 1D south shore velocity
 252 model and extrapolate the optimized model to 3D as starting model for the joint
 253 inversion. The relocation steps include an initial location with the 1D starting
 254 velocity model with a grid search approach and location refinement with the
 255 segmented bending ray-tracing technique in the joint inversion step.
 256 Errors/uncertainties in the joint inversion solution are quantified by the RMS (0.068
 257 for P-wave and 0.081 for S-wave) of the final iteration.

258 **2.3.2 Checkerboard test results**

259 Figures 3 & 4 show depth slices and cross-sectional views of the synthetic model and
 260 recovered features of the checkerboard test with the 10 km checkerboard, the catalog
 261 hypocenters, the south-shore 1D model as the starting velocity model, and 1 km grid
 262 spacing. The synthetic data inversion recovered most of the checkerboard features,
 263 particularly along the St. Lawrence River between the northeastern and
 264 southwestern limits where ray coverage is best (Fig. 2). The checkerboard recovery is
 265 best within the impact structure where most of the earthquakes occur. The
 266 recovered features are somewhat smeared northeast of the outer rim of the impact
 267 structure (Figs. 3 & 4) and throughout the edges of the region defined by the ray
 268 coverage (Fig. 2). The values of the recovered V_p and V_s changes are slightly higher
 269 (12-14%) than the input values (10%) in some sections of the upper 8 km, but there

270 is high resemblance between the synthetic (checkerboard) and recovered models,
271 particularly, down to ~ 18 -20 km (Fig. 4). The ~ 18 -20 km depth limit is consistent
272 with the distribution of the hypocenters and ray paths (Fig. 2) as the ray density
273 starts to diminish at greater depth.

274 The results of the evaluation of different parameters (starting velocity model,
275 starting earthquake location, grid spacing, and checkerboard size) can be found in
276 Figures S2 - S11. The high resemblance between the synthetic velocity model
277 (checkerboard) and the recovered model is consistent across all the three different
278 starting 1D velocity models which lends credence to the reliability of the inversion
279 algorithm and procedure. Furthermore, the checkerboard results are not affected by
280 the initial earthquake hypocenters, as the recovered checkerboard with the 3 sets of
281 hypocenter distributions and the south shore 1D starting velocity model are very
282 similar. The maximum difference in RMS between the starting hypocenter
283 distributions is 10^{-3} for both V_p and V_s . The consistency of the recovered
284 checkerboard with respect to the initial earthquake hypocenters is possible because
285 the inversion algorithm first determines absolute earthquake locations before it
286 performs joint inversion for hypocenter refinement and velocity distribution. The
287 high- and low-velocity pattern is consistent across all the tested grid spacing (0.5, 1,
288 2 km). However, the 1 km grid spacing performs better than the 0.5 and 2 km
289 spacing, as the result for the 1 km grid spacing qualitatively shows higher
290 resemblance with the synthetic model and yields the lowest RMS values (0.056 for
291 V_p ; 0.066 for V_s). The small discrepancy between the outputs for the 0.5, 1, and 2
292 km grid spacing could be due to variations in ray density per grid node.

293 The results (Figs. 3, 4, & S4 - S6) of the different checkerboard sizes show that the
294 recovered checkerboard model diminishes in resolution with decreasing size (i.e. the
295 10 km checkerboard is best resolved whereas the 4 km checkerboard is least
296 resolved). The recovered model is ostensibly well resolved down to the 5 km
297 checkerboard size but the features are completely obscured for the 4 km
298 checkerboard (Figs. S5 & S6). The difference in the result is not a shortcoming of
299 the inversion code, but may be due to changes in raypaths and ray density per node
300 as a result of the size of the checkerboard. As in the 10 km case, the resolution of
301 the recovered model for the 6 and 5 km cases is best along the St. Lawrence River
302 between the northeastern and southwestern edges of the impact structure. Similarly,

303 the vertical resolution of the 6 and 5 km checkerboards become less well resolved
 304 below \sim 18-20 km.

305 **2.4. Tomographic inversion results**

306 Figures 5 - 7 & S12 - S14 show the distribution of body wave velocities and
 307 earthquake hypocenters across the CSZ. We show five NW-SE and four NE-SW
 308 cross-sections that display V_p and V_s changes with depth (Figs. 6 & 7). Three of the
 309 NW-SE profiles run across the inner rim of the impact structure and show that
 310 velocity generally increases with depth, however with a few exceptions. Earthquake
 311 hypocenters within 1 km of each profile are projected onto the profiles. Earthquakes
 312 are diffusely distributed, especially within the impact structure, however, they follow
 313 two broader NE-SW roughly linear trends along the St. Lawrence River (Fig. 5).
 314 The two NW-SE seismicity trends sandwich a region of relatively low seismicity.
 315 Along the northern shore of St. Lawrence River, earthquakes more closely follow the
 316 outline of the major high-angle SE dipping normal faults (GRF and SLF; Figs. 1,
 317 & 5). A clearer outline of the high-angle normal faults can be seen along profiles
 318 AA' and DD' (green enclosures in Fig. 6). Within the upper 10 km, more
 319 earthquakes occur along the northern shore of St. Lawrence River than beneath the
 320 River. The distribution of seismicity across the river shows that the reactivated
 321 normal faults significantly control earthquake hypocenters in the CSZ. Although we
 322 do not observe systematic clustering of earthquakes within either lower or higher
 323 velocity bodies, visual inspection suggests that earthquakes tend to occur within
 324 lower velocity structures in some cross-sections (e.g., AA', BB' for V_s , Fig. 6). Fewer
 325 events occur inside higher velocity structures relative to the surrounding volume. A
 326 small earthquake cluster within the upper \sim 8 km in the Grenville basement off the
 327 northern shore (circled region in profiles EE' of Fig. 6) just above a high V_s body is
 328 indicative of rupture or slip within a segment of a northwest dipping fault. There is
 329 a similar earthquake cluster southeast of the central uplift between the
 330 topographically mapped boundaries of the inner and outer rims of the impact
 331 structure. This cluster also occur proximal to a high velocity body (circled region in
 332 profiles II' of Fig. 7). The earthquake clustering in the proximity of higher velocity
 333 structures suggest that the higher velocity structures are mechanically stronger (i.e.
 334 less likely to fail or are more able to accumulate seismic strain energy) similar to the
 335 conclusions of Michael and Eberhart-Phillips (1991) and Vlahovic et al. (2003).

336 A high P-wave velocity body is found northeast of the northern shore of the St.
337 Lawrence River close to the edge of the outer rim of the impact structure (Fig. 5).
338 This high velocity body has also been reported in previous studies (e.g., Vlahovic et
339 al., 2003; Powell & Lamontagne, 2017). The inner rim of the impact structure is
340 replete with low velocity bodies especially within the upper 10 km. Some of these
341 lower velocity features roughly follow the reported surface trace of the inner rim of
342 the impact structure. Below 10 km, the areal extent of these lower velocity bodies
343 decrease steadily with depth. But, a low velocity body northwest of the central
344 uplift extends down to 18 - 20 km (blue circled region in Fig. 5). However, this
345 structure is near the northwestern limit of dense ray coverage of our data set, hence
346 its depth and areal extent may not be well-constrained. Lower velocities also
347 pervade the southeast portion of the impact structure, but similar to the lower
348 velocity feature northeast of the impact structure, they are less well resolved due to
349 the locally limited ray coverage. Generally, the lower velocity features are more
350 pronounced for S-waves and somewhat more subtle for P-waves. The lower velocity
351 features appear to terminate at ~ 18 km (Profiles AA', BB', FF', GG' & HH' in
352 Figs. 6 & 7). Southeastward from profile FF' towards profile II', the lower velocity
353 features become increasingly less prominent (Fig. 7). Thus, the lower velocity
354 features are more likely related to the damaged crust due to the meteorite impact
355 rather than composition of crustal materials as they appear to be restricted within
356 the topographically mapped extent of the impact structure. The resolution of
357 structures in the 5 km checkerboard test (Fig. S5) is consistent with the
358 interpretation that lower velocity features represent realistic seismic velocity
359 variations, as their dimensions are larger than 5 km.

360 **3. Rock physics analysis and gravity modeling**

361 Following previous geophysical studies in the CSZ as well as in other seismic zones
362 (e.g., Roland et al., 2012; Powell & Lamontagne, 2017), compositional variation and
363 intense fracturing are suggested as probable cause(s) of velocity variations within
364 seismic zones. There is the possibility that one or both of the aforementioned
365 mechanisms exert significant control on velocity variations. Therefore, we also
366 investigate the influence of mechanical and compositional variation of the basement
367 rocks in the Charlevoix region on their body wave velocities, and model the gravity

368 response of such alteration to establish a quantitative relation between the
369 mechanical and compositional properties and velocity variations.

370 **3.1. Possible mechanisms for elastic moduli and density variations**

371 Variations in crustal velocity derive from changes in elastic moduli and density of
372 rock materials, and are inherently non-unique. For example, consider two rocks
373 comprised of a mixture of two mineral assemblages (phases) of comparable density,
374 but dissimilar elastic moduli. One rock contains a higher proportion of the phase
375 with larger elastic moduli. The second rock contains a mixture of the same phases,
376 but with a lower proportion of the phase with larger elastic moduli, and is also
377 permeated with fluid-filled cracks, and has a lower resulting density. The velocity
378 responses of the two example rocks types above could be similar in spite of their
379 differing densities and elastic moduli. One way to explore the tradeoff between
380 varying elastic moduli and density due to material composition and crack porosity is
381 to use the gravity response to constrain observed velocity variation.

382 We use the theoretical relation proposed by Hashin and Shtrikman (1963) for
383 multi-phase media to test the hypothesis that observed velocity variations are as a
384 result of compositional variation. Hashin and Shtrikman (1963) leveraged the
385 variational principles (principles of minimum complimentary and minimum potential
386 energies) in the theory of elasticity to derive a formulation for the lower and upper
387 bounds of the effective elastic moduli of a mechanical mixture of materials with
388 varying elastic properties. The lower and upper bounds of the bulk (K_l^* , K_u^*) and

389 shear (μ_l^* , μ_u^*) moduli of a two-phase quasi-homogeneous medium is given by:

$$390 \quad K_l^* = K_1 + \left(\frac{v_2}{\frac{1}{K_2 - K_1} + \frac{3v_1}{3K_1 + 4\mu_1}} \right) \quad (2)$$

$$391 \quad K_u^* = K_2 + \left(\frac{v_1}{\frac{1}{K_1 - K_2} + \frac{3v_2}{3K_2 + 4\mu_2}} \right) \quad (3)$$

$$392 \quad \mu_l^* = \mu_1 + \left(\frac{v_2}{\frac{1}{\mu_2 - \mu_1} + \frac{6v_1(K_1 + 2\mu_1)}{5\mu_1(3K_1 + 4\mu_1)}} \right) \quad (4)$$

$$393 \quad \mu_u^* = \mu_2 + \left(\frac{v_1}{\frac{1}{\mu_1 - \mu_2} + \frac{6v_2(K_2 + 2\mu_2)}{5\mu_2(3K_2 + 4\mu_2)}} \right) \quad (5)$$

$$394 \quad v_1 + v_2 = 1 \quad (6)$$

395

396 where K_1 , K_2 , μ_1 , μ_2 , v_1 , and v_2 are the bulk and shear moduli, and volume
 397 fraction of phases 1 and 2, respectively. The separation between the lower and upper
 398 bounds of the effective (multiphase) medium is determined by the relative stiffness
 399 of the constitutive media/phases, thus provides the extremities of the bulk and shear
 400 moduli of the multiphase quasi-homogeneous medium. The expression for a
 401 two-phase effective medium can be extended to any number of phases. Firstly, any
 402 two of the constitutive phases is treated to derive the effective medium. Then the
 403 effective medium is considered as a new, merged 'single' phase which is combined
 404 with any one of the remaining single phases to derive a new two-phase effective
 405 medium. The process is repeated until all the desired phases are added to derive an
 406 effective multiphase medium. This method enables us to mechanically mix the three
 407 most abundant basement rocks (charnockite, anorthosite, and gneiss) in the
 408 Charlevoix region (Robertson, 1968; Rivers et al., 1989) and compute the elastic
 409 moduli and density of the mixture.

410 The elastic moduli and densities of charnockite, anorthosite, gneiss were retrieved
 411 from Seront et al. (1993), Brown et al. (2016), Wang and Ji (2009), and Rao et al.
 412 (2008). Seront et al. (1993) found that anorthosite in Oklahoma, which is also

413 representative of the anorthosite in the Grenville Province, contains approximately
414 67% anorthite. Consequently, the elastic moduli of anorthosite with at least 67%
415 anorthite from Brown et al. (2016) is used here for effective media analysis. The
416 elastic properties of gneisses and charnockite in Wang and Ji (2009) and Rao et al.
417 (2008) are from type rocks in Sulu-Dabie orogenic belt, China and Tamil Nadu,
418 India, respectively, which may differ slightly from charnockites and gneisses found in
419 the Grenville Province. Nevertheless, each rock type analyzed by Rao et al. (2008)
420 contains varying degrees of the major constitutive minerals, and covers a range of
421 elastic moduli and densities. For example, the densities of the nine charnockite
422 samples in their study range from 2.689 - 2.784 g/cm³ and the Young's modulus
423 ranges from 73.44 - 88.64 GPa. We therefore assume the average of the elastic
424 properties of charnockite in Rao et al. (2008) as representative for the Grenville
425 charnockite. The densities and composition of paragneisses analyzed in Wang and Ji
426 (2009) fit the density and mineral composition of Grenville paragneiss analyzed in
427 Duncan and Garland (1977) and Volkert (2019). Therefore, we also assume the
428 elastic properties of paragneiss used in Wang and Ji (2009) here. We compute the
429 elastic moduli of an effective medium comprising charnockite, anorthosite, and gneiss
430 at different proportions (each of the rocks/phases is varied from 0 - 100%) and
431 determine a 3D density model for each rock composition model from the
432 tomographic inversion results.

433 Similar to the 3D velocity models, the resulting sparse density models would not
434 contain density predictions for areas where ray coverage is poor, rendering the
435 density model inadequate for residual gravity modeling in such areas. To address
436 inadequacy in the derived 3D density models and avoid the under-prediction of
437 gravity anomalies, we use a supervised machine learning approach, Multi-Layer
438 Perceptron (MLP) neural network, to predict density distribution for the entire 3D
439 volume of our study. The MLP algorithm can learn a non-linear function
440 approximator from the input data and use the non-linear function through
441 regression analysis to predict outcomes. We design our neural network architecture
442 with the Scikit-learn machine learning python package (Pedregosa et al., 2011). Our
443 MLP regression implementation comprises a stochastic gradient-based optimization
444 (Kingma & Ba, 2014), 3 hidden layers of 100 neurons each (100,100,100), and a
445 rectified linear unit function as the activation function for the hidden layers. The

446 optimum parameters are selected based on the score of the determination coefficient,
 447 r^2 , of the predictions from a set of trial values. We use feature scaling to ensure that
 448 the independent variables (latitude, longitude, and depth) of the input are on a
 449 similar scale to improve computation efficiency and prediction accuracy. The
 450 minimum cross-validation score (a measure of the skill of the prediction model,
 451 where a score of 1.0 indicates perfect data-matching prediction) for accepted
 452 predictions is set to 0.7. The cross-validation score of all the accepted models is
 453 typically 0.8 or greater. The cross-validation acceptance criterion results in 11 full
 454 3D density models. We account for St. Lawrence River by setting the density of the
 455 water column to 1000 kg/m^3 and a uniform water depth of 200 m which is close to
 456 the deepest bathymetry (191.1 m) in our study area
 457 (<http://gdr.agg.nrcan.gc.ca/> last accessed 17 March, 2020).

458 We use IGMAS+[©], an interactive potential field (gravity and magnetics) modeling
 459 software (Schmidt et al., 2010) to calculate the gravity anomalies, i.e., the vertical
 460 components of gravitational anomaly, of the predicted 3D density models. We
 461 retrieve a total of 2244 Bouguer anomaly measurements and 2244
 462 topography/bathymetry data for the Charlevoix region from the geophysical data
 463 repository of NRCan (<http://gdr.agg.nrcan.gc.ca/> last accessed 17 March,
 464 2020). The Bouguer anomaly data range from -67.29 to -12.95 mGal and the
 465 maximum distance between closest stations is 1.84 km (Fig. S15). We compare the
 466 modeled gravity anomaly to the observed Bouguer anomaly after upward
 467 continuation and quantify the similarity between the observed and modeled
 468 anomalies by a similarity measure, sm . The upward continuation of potential field
 469 data is necessary to isolate upper to mid-crustal ($0\text{-}20 \text{ km}$; short-wavelength)
 470 features. The sm quantifies how well the predicted gravity anomaly matches
 471 observation and it is computed as a function of the correlation distance between the
 472 observed (x) and the modeled (y) gravity anomalies as follows (Székely et al., 2007):

$$473 \quad sm = \frac{\overline{xy}}{\sqrt{(\overline{x^2} * \overline{y^2})}} \quad (7)$$

474 Higher similarity measure indicate a closer match between the modeled and observed
 475 gravity anomalies.

476 A heterogeneous porosity distribution as a result of intense fracturing, possibly due
 477 to the meteorite impact, can further contribute to the spatial variation of crustal
 478 density in the Charlevoix region. Thus, we use the theoretical formulation of Kuster
 479 and Toksöz (1974) to test the intense fracturing hypothesis. Kuster and Toksöz
 480 (1974) derived the theoretical relation between elastic moduli, material density,
 481 fracture concentration, crack geometry (i.e., aspect ratio), and body wave velocity by
 482 analysing the attenuation of elastic waves in two-phase media due to a scattering
 483 effect. The alterations (i.e., cracks) are treated as inclusions embedded in a solid
 484 matrix (i.e. 'unaltered' rock mass) and the resulting two-phase media is treated as
 485 an effective medium. It is assumed that the cracks are randomly oriented and
 486 non-interacting, and the wavelength of the propagating elastic wave is much larger
 487 than the size of the cracks. The latter condition is readily met for a spheroidal
 488 inclusion. For a single spheroidal fluid-filled crack, the theoretical formulation of
 489 Kuster and Toksöz (1974) is given by:

$$490 \quad K^* = (3K^* + 4\mu) \left(\frac{cT_{ijij}}{3} \right) \left(\frac{K' - K}{3K + 4\mu} \right) + K \quad (8)$$

$$491 \quad \mu^* = (6\mu^*(K + 2\mu) + \mu(9K + 8\mu)) \left(\frac{c(T_{ijij} - \frac{1}{3}T_{ijij})(\mu' - \mu)}{25\mu(3K + 4\mu)} \right) + \mu \quad (9)$$

$$492 \quad \rho^* = \rho(1 - c) + \rho'c \quad (10)$$

494 where $K^*, K, K', \mu^*, \mu, \mu', \rho^*, \rho, \rho', c$, and T_{ijij} & T_{ijij} are the bulk moduli of the
 495 effective medium, matrix and inclusion, shear moduli of the effective medium, matrix
 496 and inclusion, densities of the effective medium, matrix and inclusion, crack
 497 concentration (i.e. crack porosity), and functions defined by the shape of the crack,
 498 respectively (see Kuster and Toksöz (1974) for the details of T_{ijij} & T_{ijij}). For a
 499 single crack, c is equal to the crack aspect ratio, α . If the target porosity is larger
 500 than the crack aspect ratio, c is iteratively increased until the desired crack porosity
 501 is attained, i.e. crack porosity equals number of iterations multiplied by the crack
 502 aspect ratio. The above formulation allows for the determination of the influence of
 503 a wide range of crack geometries and crack porosity on seismic wave velocities. We
 504 modeled the joint effect of crack aspect ratio ($10^{-3}, 10^{-2}, 10^{-1}$), crack porosity up to
 505 0.1 due to fluid-filled crack-like fractures, and different proportions of charnockite,

506 anorthosite and gneiss on seismic wave velocity to derive a 3D density model for
 507 each scenario. For this test, the lower and upper bounds on elastic moduli of the
 508 composite media determined from the Hashin and Shtrikman (1963) are used to
 509 account for different proportions of charnockite, anorthosite and gneiss in the
 510 models. The same neural network framework and parameters that was for the
 511 compositional variation scenario are used to predict the density values for the entire
 512 3D volume of the sparse 3D density models which results in 165 full 3D density
 513 models. The approach used for the compositional variation scenario of gravity
 514 anomaly modeling and comparison of modeled and observed gravity anomalies is
 515 also used for the intense fracturing scenario.

516 **3.2. Density models and synthetic gravity anomalies**

517 The results of effective media analysis for two-phase medium (anorthosite and
 518 water-filled cracks with the Kuster and Toksöz (1974) relation; anorthosite and
 519 gneiss with the Hashin and Shtrikman (1963) relation) are shown in (Fig. 8) to
 520 illustrate changes in elastic moduli, density, and velocity with variation in rock
 521 composition, aspect ratio, and crack porosity. For the effective medium derived with
 522 the Kuster and Toksöz (1974) theoretical formulation, the bulk modulus typically
 523 drops by 50 - 80% whereas the shear modulus decreases by up to 45% for porosities
 524 up to 0.1. The drop in bulk modulus, hence V_p , is steepest for porosities up to
 525 0.025. The rate of reduction of bulk and shear moduli decreases with crack aspect
 526 ratio irrespective of the difference between the elastic moduli of the constitutive
 527 phases. The magnitude of elastic moduli reduction is inversely related to crack
 528 aspect ratio. This is because the amount of cracks required to achieve a given
 529 porosity increases with decreasing crack aspect ratio. For example, to achieve a
 530 porosity of 0.1, it would require 10 times more cracks of aspect ratio of 0.001 than
 531 cracks of aspect ratio of 0.01 which would result to greater reduction in elastic
 532 moduli. The rate of decrease in density does not vary with porosity and volume
 533 fraction because the density of the effective medium is controlled by the volume
 534 fraction of the constitutive phases as volume of the system remains constant.

535 For the effective medium derived from the Hashin and Shtrikman (1963) relation,
 536 the elastic properties of the composite medium are less affected, because the
 537 contribution of cracks and fluids to seismic wave attenuation is absent. The elastic

538 moduli of the effective medium change nonetheless because of the difference in the
539 elastic properties of the constitutive phases. The difference in magnitude between
540 the upper and lower bounds of the elastic moduli and velocities of the effective
541 medium decrease as the difference between the elastic moduli of the constitutive
542 phases decreases (Fig. 8b).

543 Densities from the effective media analysis for the study area follow the pattern of
544 the distribution of the body wave velocities (Fig. 9a, b). Generally, the densities
545 increase with depth, however, regions of lower velocity and higher densities
546 correspond to regions of lower and higher velocities, respectively. The neural
547 network regression-derived 3D enhanced density model retains most of the features
548 of the input sparse 3D density model (Fig. 9e). However, a lower density feature
549 NW of the impact structure is shifted ~ 5 km to the northwest (e.g., Fig. S17). The
550 shift may be a result of the feature being at the terminus of the section with dense
551 ray coverage, resulting in fewer data points to precisely constrain the location.
552 Features at the termini of regions of dense ray coverage are less well resolved in the
553 neural network predictions. Interestingly, lower densities at shallow depths northwest
554 of the study area that correspond to observed negative gravity anomalies are
555 predicted, despite non-availability of data for that part of the input 3D model
556 (Figs. 9a - 9d, 10a, & 10e). The compositional variation model (Figs. 9b & 9d)
557 predicts slightly higher densities than the intense fracturing model (Figs. 9a & 9c).
558 The densities of the intense fracturing model decrease southeastward from the
559 Grenville Province towards the Appalachians, consistent with the expected
560 dominance of lower density rocks in the Appalachians when compared to Grenville
561 rocks at similar depths. The density distribution appears to highlight denser
562 Grenville crustal materials underthrusting the less dense crust of the Appalachians
563 (dashed black line in Fig. 9c). The density distribution of the compositional
564 variation model does not show a clearly defined boundary between the Grenville and
565 Appalachian rocks.

566 The observed and modeled residual gravity anomalies and their similarity measures
567 are shown in (Fig. 10) for both the entire study area (a, e) and the section of the
568 study area with dense ray coverage (c, g), respectively. In the similarity measure
569 shown in Figures 10b & 10d, each vertical bar represents the percentages of
570 anorthosite, charnockite, and gneiss in the effective medium that was used to

571 estimate each density model for the intense fracturing scenario. The similarity values
572 for the compositional variation scenario (Fig. 10f & 10h) represent similarity values
573 of composite media of anorthosite and charnockite altered by addition of a third
574 phase (gneiss) for all tested models. The similarity values increase with increasing
575 quantity of charnockite and decreasing quantity of anorthosite in the composite
576 media. Larger amounts of gneiss are associated with lower similarity values,
577 suggesting that gneiss is not a prevalent rock in the study area. Conversely, larger
578 amounts of anorthosite are associated with higher similarity values, suggesting that
579 anorthosite is more prevalent in the study area.

580 The modeled gravity anomalies, especially for the intense fracturing scenario,
581 predicted important features in the observed gravity anomalies, including positive
582 gravity anomalies in the southwest, north, northeast, and negative gravity anomalies
583 east-northeast of the impact structure and in the Appalachian (Fig. 10). The sm is
584 85% & 80% for the best intense fracturing and compositional variation models and
585 68% & 73% for the poorest intense fracturing and compositional variation models,
586 respectively, for gravity anomaly predictions in areas with dense ray coverage
587 (Figs. 10d, & 10h). The sm of the gravity anomalies predicted for the entire study
588 area is lower, and the discrepancy between the sm of the gravity anomaly prediction
589 for the entire study area and the area with high ray density is probably due to
590 uncertainties in the neural network predictions. The best gravity anomaly prediction
591 for the intense fracturing scenario was calculated with the density models comprising
592 (1) 100% anorthosite, and (2) 20% anorthosite & 80% charnockite for the entire
593 study area and the area with high ray density, respectively, with cracks of 0.1 aspect
594 ratio and up to 10% fluid-filled porosity (Figs. 10a & 10c). The best gravity
595 anomaly prediction for the compositional variation scenario was calculated with the
596 density model of a rock volume composed of a composite media (phase 1)
597 comprising 20% anorthosite & 80% charnockite, and 10% anorthosite & 90%
598 charnockite altered with gneiss (phase 2) for the entire study area and the area with
599 high ray density, respectively (Figs. 10e & 10g). The anorthosite, charnockite, and
600 gneiss contents of the 5 best model of the intense fracturing scenario range from
601 10-100%, 0-90% & 0-30%, and 10-90%, 0-90% & 0-20% for the entire study area and
602 the section with high ray density, respectively (Figs. S18 - S21).

603 Gravity anomalies west of the North shore of St. Lawrence River are mostly
604 positive, whereas the gravity anomalies east of the northern shore are negative for
605 both the observed and modeled data. This is because of the mass deficiency over St.
606 Lawrence River and the lower density Appalachian rocks. The negative gravity
607 anomalies northwest of the impact structure is an exception to this general
608 observation and could be due to the presence of a less dense rock isolated among
609 denser rocks. There are no structural features that show large scale mass deficiency
610 that might be responsible for the negative gravity anomaly (Fig. S16). Alternatively,
611 the negative gravity anomaly could be an artifact of data sparsity, as there are few
612 observations within the area (Fig. S15a).

613 4. Discussion

614 4.1. Importance of robust tomographic resolution test

615 The multi-faceted approach to the travel-time tomography problem in this paper
616 addresses several sources of bias, including forward solver, source-station geometries,
617 starting velocity model, and noise. For example, the checkerboard test enables
618 disregarding potential sources of error in the synthetic travel-time predictions,
619 because the forward solver and model parameterization in the synthetic data set
620 travel-time prediction algorithm (*Tomodd*) are different from those used for the
621 inversion (*LOTOS*). Furthermore, using different source-receiver geometries in the
622 synthetic travel-time computation and their reconstruction helps ensure the
623 robustness of the tomographic inversion procedure and improve reliability of the
624 results. For example, the earthquake hypocenters are set to arbitrary locations
625 within the 3D volume prescribed in the checkerboard reconstruction with noise
626 added to the synthetic travel times. We also test different model grid sizes and 1D
627 starting velocity models, including a randomized 1D model, where the recovered
628 checkerboard models are consistent in all cases (Figs. 3, 4, & S2 - S11). The
629 travel-time tomography setup and approach are designed to identify and resolve
630 biases from possible errors in forward solvers, and inversion routines that are often
631 masked and unidentified with too much *a priori* information. This approach
632 subjects the synthetic travel times to the conditions of real data as much as possible.

633 Subjecting synthetic data to the conditions of a real data does not aim to further
634 impose nonuniqueness in the solution, because seismic tomography solutions are
635 inherently nonunique, even for overdetermined problems (Rawlinson et al., 2014).
636 Rather, the objective is to evaluate the aptness of the algorithm to resolve features
637 buried in noisy data (i.e., data with some imprecise arrival time picks and/or
638 erroneous origin times). Figures S5 & S6 show that structural features on the scale
639 of 5 km or larger can be resolved, such as the lower velocities observed within the
640 impact structure (Figs. 5 - 7) that likely highlight highly fractured crustal rocks.

641 **4.2. Zones of weakness in the CSZ**

642 The distribution of earthquake hypocenters in the CSZ highlights complex fault
643 structures developed from the tectonic history and the overprinting of the meteorite
644 impact. Previous studies (e.g., Yu et al., 2016; Onwuemeka et al., 2018) noted that
645 earthquakes are more diffusely distributed within the impact structure due to a
646 highly fractured volume, especially within the upper 20 km. The earthquake
647 epicenters broadly show two northeast-southwest alignments with more scatter
648 within the impact structure (Fig. 5 - 7 & S12). The depth of the earthquakes
649 increases towards the northeast outside of the impact structure and towards the
650 southeast. As the impact structure is hypothesized to form a bowl-shaped structure
651 that decreases in depth away from the center, the deeper events possibly highlight
652 the extent of active faulting processes on the planes of the Iapetus rift faults. A
653 region of lower seismicity between the two broad northeast-southwest seismicity
654 belts (Fig. 5) may indicate accumulated strain energy is released in aseismic
655 deformation modes, or strain accumulation that may be released in a large event.

656 Despite a diffuse distribution within the impact structure, earthquakes around the
657 northern shoreline highlight southeastward dipping faults (green circled region in
658 Figure 6). The distribution of earthquakes across profiles AA' and BB' in Figure 6
659 describes what could be an outline of the more damaged segment of the impact
660 region. Further northwest, the hypocenters project onto what is possibly the Gouffre
661 River Fault plane. The southeast dipping hypocenter distribution is particularly clear
662 on profiles that are further away from the center of the impact structure. The trend
663 of the hypocenters shown in Fig. 6 indicates that at least the Gouffre River Fault,
664 and possibly the St. Lawrence and Charlevoix faults (Fig. 1), are high-angle normal

665 faults dipping at $\sim 60^\circ$ SE that likely developed during the breakup of
666 supercontinent Rodinia (Kumarapeli & Saull, 1966) and was reactivated in a reverse
667 sense under the current stress regime. The geodynamic model of Fadugba et al.
668 (2019) indicates that the St. Lawrence rift fault dips by up to 70° within the
669 vicinity of the CSZ. Yu et al. (2016) made a similar interpretation of high-angle
670 dipping normal faults, namely, the Gouffre River, St. Lawrence, and Charlevoix
671 faults, based on the distribution of relocated seismicity. Thus, the relocated
672 seismicity distribution from our joint inversion is consistent with the results from
673 independent methods, and likely elucidates the geometry of the major seismogenic
674 faults in the CSZ.

675 **4.3. Constraints on velocity variations**

676 Several regions of high and low velocities are elucidated within the CSZ and are
677 clearly associated with earthquake hypocenters (Fig. 6). The velocity variation is
678 consistent with the complexity of the crust due to the many tectonic events that
679 significantly altered the rocks and created distributed faults and fracture systems.
680 Higher velocities are observed northeast of the inner rim of the impact structure at
681 mid-crustal depth and lower velocities are ubiquitous within it due to a shattered
682 crust. The higher velocity region does not correlate with higher Bouguer anomaly,
683 and is probably due to rock bodies of comparable density with surrounding rock
684 masses but of higher elastic moduli. For example, the density of anorthosite (2720
685 kg/m^3) is comparable to the density of charnockite ($2735 kg/m^3$); a density contrast
686 of $15 kg/m^3$ would produce a negligible gravity anomaly. For instance, the spherical
687 equivalent of a structure with dimension of about 20 km length, 15 km width, and 8
688 km thick, and assuming density contrast of $15 kg/m^3$ would produce a gravity
689 anomaly of 1.8 mGal. However, the elastic moduli of anorthosite and charnockite are
690 sufficiently different to yield a velocity contrast of at least 12%. Therefore, the
691 velocity variation northeast of the impact structure is most likely due to
692 compositional variation with the effective medium composed of anorthosite and
693 charnockite or rocks of similar contrast in mechanical and elastic properties.
694 Earthquakes of larger magnitudes occur within or around this higher velocity region
695 (e.g., Vlahovic et al., 2003), which suggests it is comprised of rocks that are
696 mechanically stronger hence, able to accumulate more strain energy than the

697 surrounding material. Michael and Eberhart-Phillips (1991) studied relations
698 between material properties of rocks and fault behaviour on the San Andreas fault
699 system. The authors constrained the 3D V_p model and found that regions of high
700 V_p correlate with high moment release and have a higher propensity to accumulate
701 strain energy which is subsequently released in larger events. Our interpretation of
702 the mechanical strength of the high velocity body are consistent with the studies
703 cited above.

704 The lower V_p and V_s values observed within the inner rim of the impact structure
705 are seismic manifestation of damaged CSZ crust due to either prevalence of high
706 crack density/porosity, low aspect ratio cracks, varying quartz and feldspar
707 concentration, or a combination of the above factors (Christensen & Mooney, 1995;
708 Christensen, 1996). For example, low aspect ratio cracks disproportionately lower
709 P-wave velocities in comparison to S-wave velocities due to larger decreases in the
710 bulk modulus relative to the shear modulus (e.g., Shearer, 1988), and typically result
711 in lower V_p/V_s ratios. High crack density reduces both V_p and V_s , and depending
712 on the volume of the void space in the cracks and anisotropy, V_s may be
713 disproportionately lower than V_p . Rocks rich in plagioclase feldspar exhibit higher
714 Poisson's ratios, hence higher V_p/V_s than granitic rocks due to high anorthite and
715 quartz contents, respectively (Christensen, 1996). The lower V_s and high V_p/V_s
716 observed within the impact structure (Figs. 5 - 7, S13 & S14) would suggest high
717 crack density, low quartz and high anorthite content, and high aspect ratio cracks.
718 However, among all the density models tested, the effective medium comprising
719 cracks of aspect ratio corresponding to 0.1, low quartz and high anorthite
720 concentration produce residual gravity anomalies that best fit the observations
721 (Figs. 9 & 10), which indicate that though the aspect ratio is low, high crack density
722 and high anorthite concentration are dominant causative mechanisms for the
723 observed high V_p/V_s values. The low quartz content interpretation is in agreement
724 with what Figures 10c & 10d clearly show that similarity measure increases with
725 decreasing gneiss content.

726 Several studies have suggested that observed velocity variations in the CSZ,
727 especially within the impact structure, could be due to high pore-pressure, high
728 crack density, and/or compositional variation. For example, Powell and Lamontagne
729 (2017) postulate that compositional variation models best explain several observed

730 velocity variations in the CSZ. Powell and Lamontagne (2017) further suggests that
731 increased pore pressure in cracks with high aspect ratios explains observed seismicity
732 and low V_p/V_s especially within the upper 8 km along the eastern rim of the impact
733 structure. Similar to Powell and Lamontagne (2017), we find that V_p/V_s values in
734 the upper 9-10 km within the impact structure are 1.7 or lower but higher below the
735 upper 9-10 km which could be due to the generally observed phenomenon of
736 increasing V_p/V_s with depth as silica content decreases (e.g., Christensen &
737 Mooney, 1995; Christensen, 1996). The unusually high V_p/V_s ratio below 10 km
738 could be due to disproportionately higher V_p relative to V_s within the impact
739 structure, which supports our proposition that a combination of low crack aspect
740 ratio and high crack density due to the meteorite impact, and increasing anorthite
741 content better explain observed velocity variations. Although, in general, seismic
742 velocities decrease with increasing crack density (e.g., Hadley, 1976), decreasing
743 quartz and increasing anorthite content could dominate and produce higher V_p/V_s
744 values. Furthermore, in subduction zones, it has been observed that high V_p/V_s is
745 associated with overpressured rock with the increased fluid content originating from
746 dehydration of hydrous minerals from subducting oceanic crust and mantle at
747 shallow depth and serpentinization deeper in the subduction zone (e.g., Peacock,
748 1990; Audet et al., 2009). However such mechanisms and conditions for transport of
749 water to depth greater than ~ 10 km is non-existent in the CSZ, and there is
750 currently no active regional metamorphism in Grenville Province. Consequently,
751 precipitation of fluid due to metamorphic alterations is not ongoing. Also, the range
752 of stress drop values (2-200 MPa; majority of the stress drop values are between 10
753 and 100 MPa) reported for the CSZ indicates that high pore pressure is unlikely
754 present during CSZ earthquake ruptures (Onwuemeka et al., 2018). Therefore,
755 assumptions of high pore-pressure as the main mechanism of fault strength
756 reduction does not adequately explain earthquake processes and velocity variation in
757 the CSZ.

758 Mazzotti and Townend (2010) considered two scenarios that could explain observed
759 maximum horizontal (S_H) stress re-orientation in the St. Lawrence rift system: (1)
760 high coefficient of friction and low pore pressure, which implies differential stress
761 perturbations of 160-250 MPa, and (2) low coefficient of friction or high pore
762 pressure which implies stress perturbations of up to ~ 20 -40 MPa at

763 mid-seismogenic depths. Given that post-glacial isostatic rebound stress is probably
764 a major source of stress perturbation in the CSZ (Wu & Hasegawa, 1996; Tarayoun
765 et al., 2018), albeit low in magnitude (~ 10 MPa), post-glacial rebound stresses
766 would require stress amplification to raise fault loading stress high enough to
767 overcome fault strength. Onwuemeka et al. (2018) found that stress drop values
768 within the impact structure could be more than one order of magnitude higher than
769 stress drop values of earthquakes located outside of it, which implies that faults
770 within the structure, most of which are related to the meteorite impact, are less
771 mature with relatively stronger asperities than the paleorift faults prevalent outside
772 the structure. Stronger asperity, typical of immature faults, is a fault strength
773 enhancement ingredient (e.g., Viegas et al., 2010). Stronger faults would require
774 higher stress levels, especially in the absence of elevated pore pressure, to overcome
775 frictional strength and initiate slip which could result in higher stress drops. The
776 stress drop discrepancy clearly shows that seismogenic faults within the impact
777 structure exhibit a high coefficient of friction consistent with the low pore pressure
778 and high coefficient of friction model invoked by Mazzotti and Townend (2010) as a
779 possible explanation for S_H re-orientation in the CSZ. Given that intense fracturing
780 due to tectonic inheritance can amplify crustal stresses by up to a factor of 10 (e.g.,
781 Mazzotti & Townend, 2010), stress perturbation under the condition of high
782 frictional coefficient and low pore-pressure is sufficient to explain observed maximum
783 horizontal stress re-orientation in the CSZ, thus offering another piece of evidence
784 that suggests crustal weakening due to intense fracturing explains velocity variations
785 and the seismicity distribution within the impact structure (Figs. 9 & 10). Outside
786 the impact structure, observed velocity variations are more related to compositional
787 variation rather than intense fracturing. Therefore, our effective media analysis
788 points to different dominant mechanisms for the spatial variations of seismic velocity
789 in the CSZ.

790 5. Conclusion

791 To achieve robust assessment of tomography inversion algorithms and reliable
792 results, we propose a checkerboard test methodology where synthetic travel-times
793 are predicted with a forward solver that is different from the forward solver in the
794 inversion framework. Furthermore, synthetic travel-times must be subjected to the

795 conditions of real data, for example, by adding noise, using different source-station
796 geometry, and using a starting velocity model that is different from the checkered
797 synthetic velocity model. Such an approach yields a more unbiased report of the
798 robustness of the tomographic inversion framework.

799 Applying the methodology to a joint tomography inversion for the Charlevoix
800 Seismic Zone in eastern Canada, we find that relocated hypocenters broadly define
801 two NE-SW seismicity clusters separated by a region of lower seismicity, which is
802 probably due a general lack of seismically active faults or faults that exhibit aseismic
803 deformation modes. The hypocenters image what is likely SE-dipping Iapetan
804 normal faults, namely Gouffre River, St. Lawrence and Charlevoix faults, among
805 other possible fault structures, and the normal faults are disrupted within the
806 impact structure. The westernmost imaged fault structure (Gouffre River Fault)
807 dips $\sim 60^\circ$ SE, consistent with the dip angles reported in previous studies. More
808 distributed seismicity within the impact structure is related to highly damaged crust
809 due to a late Ordovician to early Silurian meteorite impact. Lower velocity
810 structures are ubiquitous within the impact structure, which is consistent with
811 seismic velocity reduction due to a heavily damaged crust. A higher velocity region
812 northeast of the impact structure boundary represent a more competent crust and is
813 associated with larger magnitude events due to its greater propensity for strain
814 energy accumulation. This higher velocity region is indicative of a conglomeration
815 of at least two rocks (e.g., anorthosite and charnockite) of similar density but
816 disparate elastic moduli, as there is no discernible gravity anomaly with the
817 surrounding rocks.

818 Effective media analysis and gravity modeling reduced non-uniqueness in the
819 tomography results and helped constrain the physical mechanisms (i.e.,
820 compositional variation and intense fracturing) that dominate velocity variations in
821 the CSZ. Velocity variations within the impact structure can be explained by highly
822 fractured crust replete with cracks of ~ 0.1 aspect ratio with porosity enhancement
823 of up to 10%. Outside the impact structure, compositional variations control seismic
824 velocities. Therefore, intense fracturing and compositional variation strongly
825 influence velocity variations and thereby seismogenesis in the CSZ, rendering
826 elevated pore fluid pressure a less likely dominant mechanism.

827 **Acknowledgments**

828 The authors are grateful to Dr. Sabine Schmidt and Dr. Hans-Jürgen Götze for
 829 providing a free copy of their potential field modeling software, *IGMAS+*[©]. We
 830 thank Dr. Ivan Koulakov for sharing the latest version of his 3D tomographic
 831 inversion code, *LOTOS*. Older versions of *LOTOS* are available at
 832 <http://www.ivan-art.com/science/LOTOS/>. All numerical computations were
 833 performed with open-source software, *Python*[©]. We thank Pierre Arch his assistance
 834 in the maintenance of the McGill stations in Charlevoix. We acknowledge
 835 earthquake catalog, Bouguer anomaly and bathymetry data from NRCan ([https://](https://www.earthquakescanada.nrcan.gc.ca/stndon/AutoDRM/autodrm_req-en.php)
 836 www.earthquakescanada.nrcan.gc.ca/stndon/AutoDRM/autodrm_req-en.php and
 837 <http://gdr.agg.nrcan.gc.ca/>), and waveform data from Incorporated Research
 838 Institutions for Seismology
 839 (<http://ds.iris.edu/gmap/#network=X8,CN&planet=earth>). Relocated
 840 hypocenters and the 3D velocity model presented in this paper can be accessed at
 841 <http://www.eps.mcgill.ca/~jonwueme/out/CSZ02/>. This work is supported by
 842 the Team Research Program of the Fonds de Recherche du Québec–Nature et
 843 Technologies (PR-191259).

844 **References**

- 845 Audet, P., Bostock, M. G., Christensen, N. I., & Peacock, S. M. (2009). Seismic
 846 evidence for overpressured subducted oceanic crust and megathrust fault
 847 sealing. *Nature*, *457*(7225), 76–78.
- 848 Baird, A., McKinnon, S., & Godin, L. (2010). Relationship between structures,
 849 stress and seismicity in the charlevoix seismic zone revealed by 3-d
 850 geomechanical models: Implications for the seismotectonics of continental
 851 interiors. *Journal of Geophysical Research: Solid Earth*, *115*(B11).
- 852 Bendick, R., Bilham, R., Fielding, E., Gaur, V., Hough, S., Kier, G., . . . Mukul, M.
 853 (2001). The 26 january 2001 “republic day” earthquake, india. *Seismological*
 854 *Research Letters*, *72*(3), 328–335.
- 855 Brown, J. M., Angel, R. J., & Ross, N. L. (2016). Elasticity of plagioclase feldspars.
 856 *Journal of Geophysical Research: Solid Earth*, *121*(2), 663–675.
- 857 Christensen, N. I. (1996). Poisson’s ratio and crustal seismology. *Journal of*
 858 *Geophysical Research: Solid Earth*, *101*(B2), 3139–3156.

- 859 Christensen, N. I., & Mooney, W. D. (1995). Seismic velocity structure and
 860 composition of the continental crust: A global view. *Journal of Geophysical*
 861 *Research: Solid Earth*, 100(B6), 9761–9788.
- 862 Dineva, S., Eaton, D., Ma, S., & Mereu, R. (2007). The october 2005 georgian bay,
 863 canada, earthquake sequence: Mafic dykes and their role in the mechanical
 864 heterogeneity of precambrian crust. *Bulletin of the Seismological Society of*
 865 *America*, 97(2), 457–473.
- 866 Duncan, P., & Garland, G. (1977). A gravity study of the saguenay area, quebec.
 867 *Canadian Journal of Earth Sciences*, 14(2), 145–152.
- 868 Ebel, J. E., Bonjer, K.-P., & Oncescu, M. C. (2000). Paleoseismicity: Seismicity
 869 evidence for past large earthquakes. *Seismological Research Letters*, 71(2),
 870 283–294.
- 871 Fadugba, O. I., Choi, E., & Powell, C. A. (2019). Effects of preexisting structures on
 872 the seismicity of the charlevoix seismic zone. *Journal of Geophysical Research:*
 873 *Solid Earth*, 124(7), 7370–7386.
- 874 Gordon, R. G. (1998). The plate tectonic approximation: Plate nonrigidity, diffuse
 875 plate boundaries, and global plate reconstructions. *Annual Review of Earth*
 876 *and Planetary Sciences*, 26(1), 615–642.
- 877 Hadley, K. (1976). Comparison of calculated and observed crack densities and
 878 seismic velocities in westerly granite. *Journal of Geophysical Research*, 81(20),
 879 3484–3494.
- 880 Hashin, Z., & Shtrikman, S. (1963). A variational approach to the theory of the
 881 elastic behaviour of multiphase materials. *Journal of the Mechanics and*
 882 *Physics of Solids*, 11(2), 127–140.
- 883 Hough, S. E., et al. (2004). Scientific overview and historical context of the 1811-
 884 1812 new madrid earthquake sequence. *Annals of Geophysics*.
- 885 Kingma, D. P., & Ba, J. (2014). Adam: A method for stochastic optimization. *arXiv*
 886 *preprint arXiv:1412.6980*.
- 887 Kissling, E., Ellsworth, W., Eberhart-Phillips, D., & Kradolfer, U. (1994). Initial
 888 reference models in local earthquake tomography. *Journal of Geophysical*
 889 *Research: Solid Earth*, 99(B10), 19635–19646.
- 890 Koulakov, I. (2009a). Lotos code for local earthquake tomographic inversion:
 891 Benchmarks for testing tomographic algorithms. *Bulletin of the Seismological*

- 892 *Society of America*, 99(1), 194–214.
- 893 Koulakov, I., Bohm, M., Asch, G., Lühr, B.-G., Manzanares, A., Brotopuspito, K.,
894 ... others (2007). P and s velocity structure of the crust and the upper mantle
895 beneath central java from local tomography inversion. *Journal of Geophysical*
896 *Research: Solid Earth*, 112(B8).
- 897 Koulakov, I., Kaban, M., Tesauro, M., & Cloetingh, S. (2009b). P-and s-velocity
898 anomalies in the upper mantle beneath europe from tomographic inversion of
899 isc data. *Geophysical Journal International*, 179(1), 345–366.
- 900 Kumarapeli, P., & Saull, V. A. (1966). The st. lawrence valley system: a north
901 american equivalent of the east african rift valley system. *Canadian Journal of*
902 *Earth Sciences*, 3(5), 639–658.
- 903 Kuster, G. T., & Toksöz, M. N. (1974). Velocity and attenuation of seismic waves in
904 two-phase media: Part i. theoretical formulations. *Geophysics*, 39(5), 587–606.
- 905 Lamontagne, M. (1999). Rheological and geological constraints on the earthquake
906 distribution in the charlevoix seismic zone, quebec, canada. *Ph.D. thesis,*
907 *Carleton University, (Geological Survey of Canada Open File Report D-3778)*.
- 908 Lemieux, Y., Tremblay, A., & Lavoie, D. (2003). Structural analysis of supracrustal
909 faults in the charlevoix area, quebec: relation to impact cratering and the
910 st-laurent fault system. *Canadian Journal of Earth Sciences*, 40(2), 221–235.
- 911 Liu, M., & Stein, S. (2016). Mid-continental earthquakes: Spatiotemporal
912 occurrences, causes, and hazards. *Earth-Science Reviews*, 162, 364–386.
- 913 Ma, S., & Eaton, D. W. (2007). Western quebec seismic zone (canada): Clustered,
914 midcrustal seismicity along a mesozoic hot spot track. *Journal of Geophysical*
915 *Research: Solid Earth*, 112(B6).
- 916 Mazzotti, S. (2007). Geodynamic models for earthquake studies in intraplate north
917 america. *SPECIAL PAPERS-GEOLOGICAL SOCIETY OF AMERICA*, 425,
918 17.
- 919 Mazzotti, S., & Adams, J. (2005). Rates and uncertainties on seismic moment and
920 deformation in eastern canada. *Journal of Geophysical Research: Solid Earth*,
921 110(B9).
- 922 Mazzotti, S., & Gueydan, F. (2018). Control of tectonic inheritance on continental
923 intraplate strain rate and seismicity. *Tectonophysics*, 746, 602–610.
- 924 Mazzotti, S., & Townend, J. (2010). State of stress in central and eastern north

- 925 american seismic zones. *Lithosphere*, 2(2), 76–83.
- 926 Michael, A. J., & Eberhart-Phillips, D. (1991). Relations among fault behavior,
 927 subsurface geology, and three-dimensional velocity models. *Science*, 253(5020),
 928 651–654.
- 929 Nuttli, O. W. (1973). Seismic wave attenuation and magnitude relations for eastern
 930 north america. *Journal of Geophysical Research*, 78(5), 876–885.
- 931 Onwuemeka, J., Liu, Y., & Harrington, R. M. (2018). Earthquake stress drop in the
 932 charlevoix seismic zone, eastern canada. *Geophysical Research Letters*, 45(22),
 933 12–226.
- 934 Peacock, S. A. (1990). Fluid processes in subduction zones. *Science*, 248(4953),
 935 329–337.
- 936 Pedregosa, F., Varoquaux, G., Gramfort, A., Michel, V., Thirion, B., Grisel, O., ...
 937 Duchesnay, E. (2011). Scikit-learn: Machine learning in Python. *Journal of*
 938 *Machine Learning Research*, 12, 2825–2830.
- 939 Powell, C. A., & Lamontagne, M. (2017). Velocity models and hypocenter
 940 relocations for the charlevoix seismic zone. *Journal of Geophysical Research:*
 941 *Solid Earth*, 122(8), 6685–6702.
- 942 Rao, M., Lakshmi, K. P., Chary, K., & Vijayakumar, N. (2008). Elastic properties
 943 of charnockites and associated granitoid gneisses of kudankulam, tamil nadu,
 944 india. *Current Science*, 1285–1291.
- 945 Rawlinson, N., Fichtner, A., Sambridge, M., & Young, M. K. (2014). Seismic
 946 tomography and the assessment of uncertainty. In *Advances in geophysics*
 947 (Vol. 55, pp. 1–76). Elsevier.
- 948 Rivers, T., Martignole, J., Gower, C., & Davidson, A. (1989). New tectonic divisions
 949 of the grenville province, southeast canadian shield. *Tectonics*, 8(1), 63–84.
- 950 Robertson, P. (1968). La malbaie structure, quebec—a palaeozoic meteorite impact
 951 site. *Meteoritics*, 4(2), 89–112.
- 952 Roland, E., Lizarralde, D., McGuire, J. J., & Collins, J. A. (2012). Seismic velocity
 953 constraints on the material properties that control earthquake behavior at
 954 the quebrada-discovery-gofar transform faults, east pacific rise. *Journal of*
 955 *Geophysical Research: Solid Earth*, 117(B11).
- 956 Rondot, J. (1971). Impactite of the charlevoix structure, quebec, canada. *Journal of*
 957 *Geophysical Research*, 76(23), 5414–5423.

- 958 Schmidt, S., Götze, H.-J., Fichler, C., & Alvers, M. (2010). Igmast—a new 3d
 959 gravity, ftg and magnetic modeling software. *GEO-INFORMATIK Die Welt
 960 im Netz*, edited by: Zipf, A., Behncke, K., Hillen, F., and Scheffermeyer, J.,
 961 *Akademische Verlagsgesellschaft AKA GmbH, Heidelberg, Germany*, 57–63.
- 962 Schmieder, M., Shaulis, B. J., Lapen, T. J., Buchner, E., & Kring, D. A. (2019).
 963 In situ u–pb analysis of shocked zircon from the charlevoix impact structure,
 964 québec, canada. *Meteoritics & Planetary Science*.
- 965 Seront, B., Mainprice, D., & Christensen, N. I. (1993). A determination of the three-
 966 dimensional seismic properties of anorthosite: Comparison between values
 967 calculated from the petrofabric and direct laboratory measurements. *Journal
 968 of Geophysical Research: Solid Earth*, 98(B2), 2209–2221.
- 969 Shearer, P. M. (1988). Cracked media, poisson’s ratio and the structure of the upper
 970 oceanic crust. *Geophysical Journal International*, 92(2), 357–362.
- 971 Sykes, L. R. (1978). Intraplate seismicity, reactivation of preexisting zones of
 972 weakness, alkaline magmatism, and other tectonism postdating continental
 973 fragmentation. *Reviews of Geophysics*, 16(4), 621–688.
- 974 Székely, G. J., Rizzo, M. L., Bakirov, N. K., et al. (2007). Measuring and testing
 975 dependence by correlation of distances. *The annals of statistics*, 35(6), 2769–
 976 2794.
- 977 Tarayoun, A., Mazzotti, S., Craymer, M., & Henton, J. (2018). Structural
 978 inheritance control on intraplate present-day deformation: Gps strain rate
 979 variations in the saint lawrence valley, eastern canada. *Journal of Geophysical
 980 Research: Solid Earth*, 123(8), 7004–7020.
- 981 Tuttle, M. P., & Atkinson, G. M. (2010). Localization of large earthquakes in
 982 the charlevoix seismic zone, quebec, canada, during the past 10,000 years.
 983 *Seismological Research Letters*, 81(1), 140–147.
- 984 Um, J., & Thurber, C. (1987). A fast algorithm for two-point seismic ray tracing.
 985 *Bulletin of the Seismological Society of America*, 77(3), 972–986.
- 986 Viegas, G., Abercrombie, R. E., & Kim, W.-Y. (2010). The 2002 m5 au sable
 987 forks, ny, earthquake sequence: Source scaling relationships and energy budget.
 988 *Journal of Geophysical Research: Solid Earth*, 115(B7).
- 989 Vlahovic, G., Powell, C., & Lamontagne, M. (2003). A three-dimensional p wave
 990 velocity model for the charlevoix seismic zone, quebec, canada. *Journal of*

- 991 *Geophysical Research: Solid Earth*, 108(B9).
- 992 Volkert, R. A. (2019). Constraints from geochemistry and field relationships for the
993 origin of kornerupine-bearing gneiss from the grenvillian new jersey highlands
994 and implications for the source of boron. *Minerals*, 9(7), 431.
- 995 Wang, Q., & Ji, S. (2009). Poisson's ratios of crystalline rocks as a function of
996 hydrostatic confining pressure. *Journal of Geophysical Research: Solid Earth*,
997 114(B9).
- 998 Wu, P., & Hasegawa, H. S. (1996). Induced stresses and fault potential in eastern
999 canada due to a realistic load: a preliminary analysis. *Geophysical Journal
1000 International*, 127(1), 215–229.
- 1001 Yu, H., Liu, Y., Harrington, R. M., & Lamontagne, M. (2016). Seismicity along
1002 st. lawrence paleorift faults overprinted by a meteorite impact structure in
1003 charlevoix, québec, eastern canada. *Bulletin of the Seismological Society of
1004 America*, 106(6), 2663–2673.
- 1005 Zhang, H., & Thurber, C. H. (2003). Double-difference tomography: The
1006 method and its application to the hayward fault, california. *Bulletin of the
1007 Seismological Society of America*, 93(5), 1875–1889.

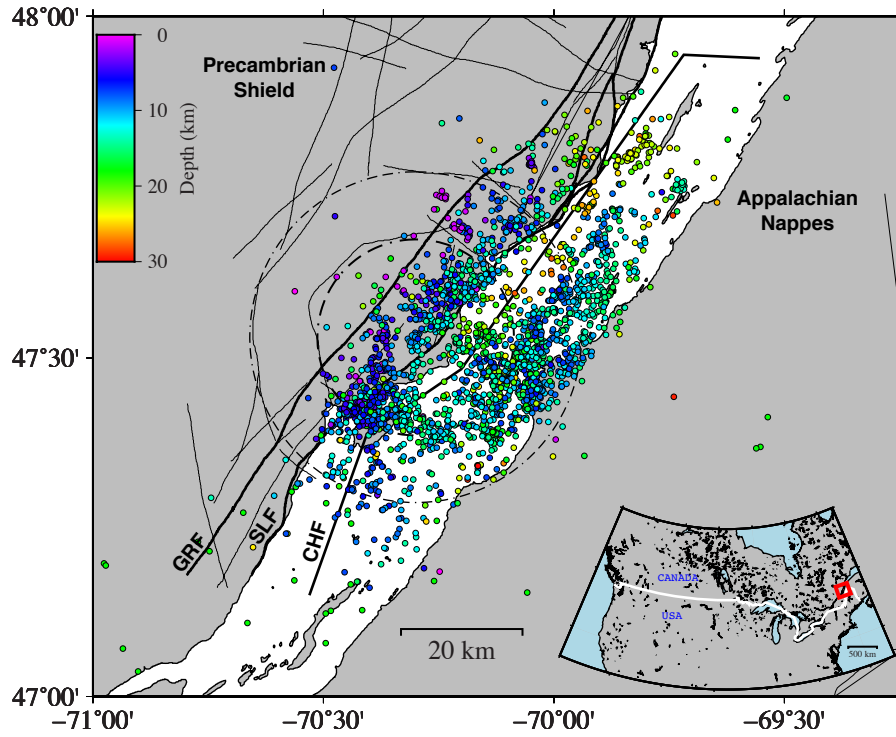


Figure 1. Distribution of 2405 earthquakes reported by Natural Resources Canada (NRCAN) between January 1988 and March 2019 color-coded by depth. Dashed circles represent the inner and outer rims of the Charlevoix meteorite impact structure originally mapped by Rondot (1971). CHF, GRF, and SLF correspond to Charlevoix, Gouffre River, and St. Lawrence faults, some of the major normal faults of the St. Lawrence rift system (e.g., Yu et al., 2016). Bottom-right inset: Red box represents the location of the study area within the North American continent.

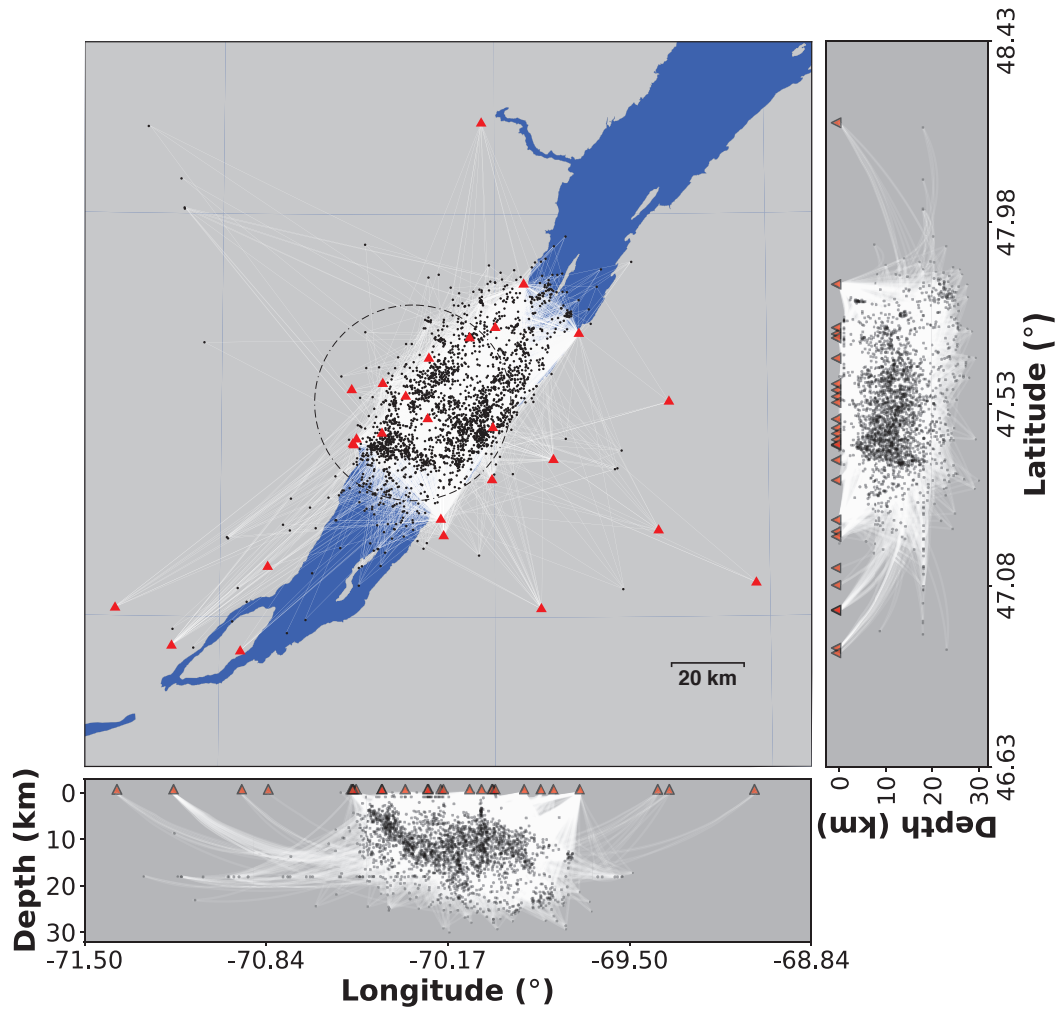


Figure 2. Ray density of the study area. White lines, black dots, and red triangles represent ray paths, earthquakes, and seismic stations respectively. Blue area denotes the St. Lawrence River. Depth cross-sectional views of ray density are shown to the right and at the bottom.

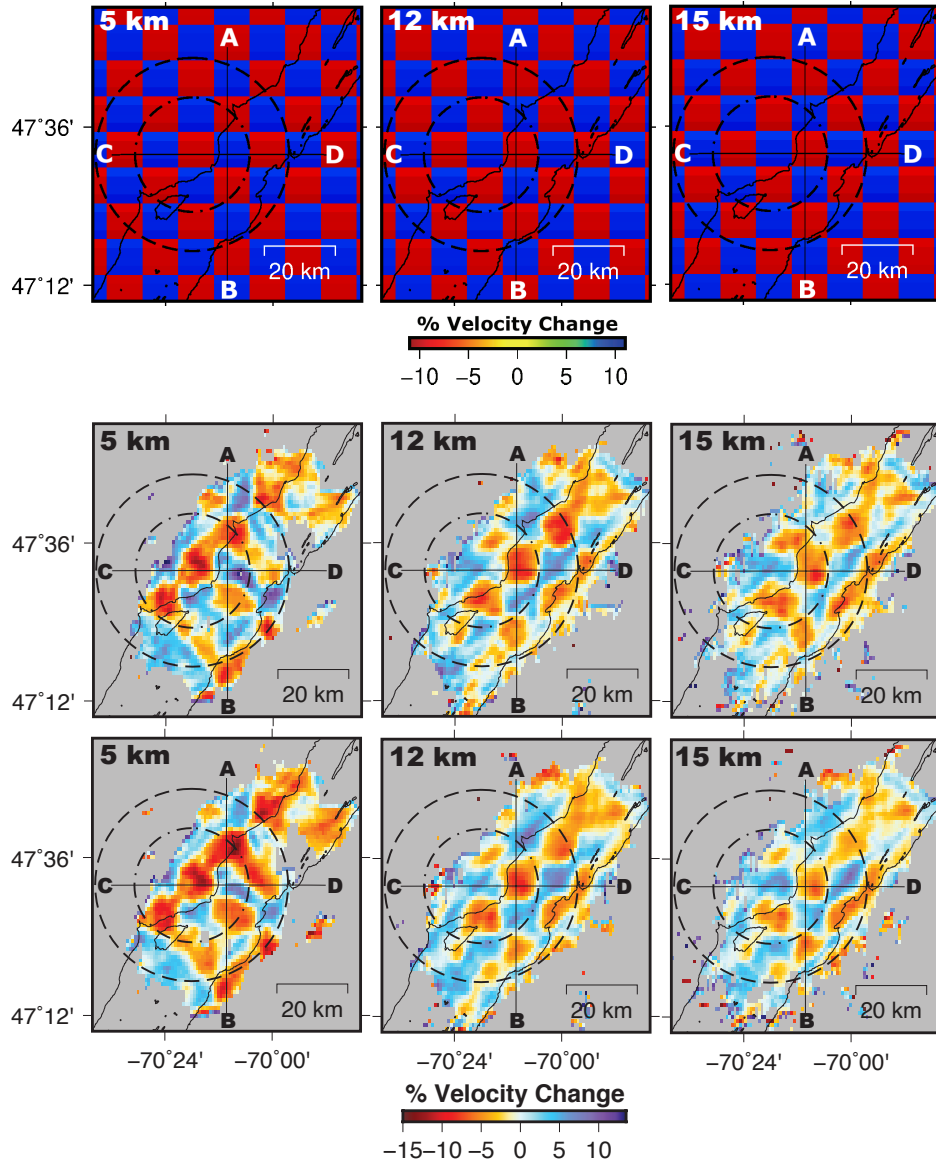


Figure 3. Checkerboard resolution test results for 10 km (left panel), 12 km (middle panel), and 15 km (right panel) depth slices. The top panel shows depth slices of the input model and the blocks (10×10 km each) represent $\pm 10\%$ alternating perturbations of the south shore 1D velocity model of Lamontagne (1999). The middle and bottom panels are the recovered checkerboard for P-waves and S-waves variations respectively. Vertical cross-sections along Profiles AB and CD are shown in Fig. 4.

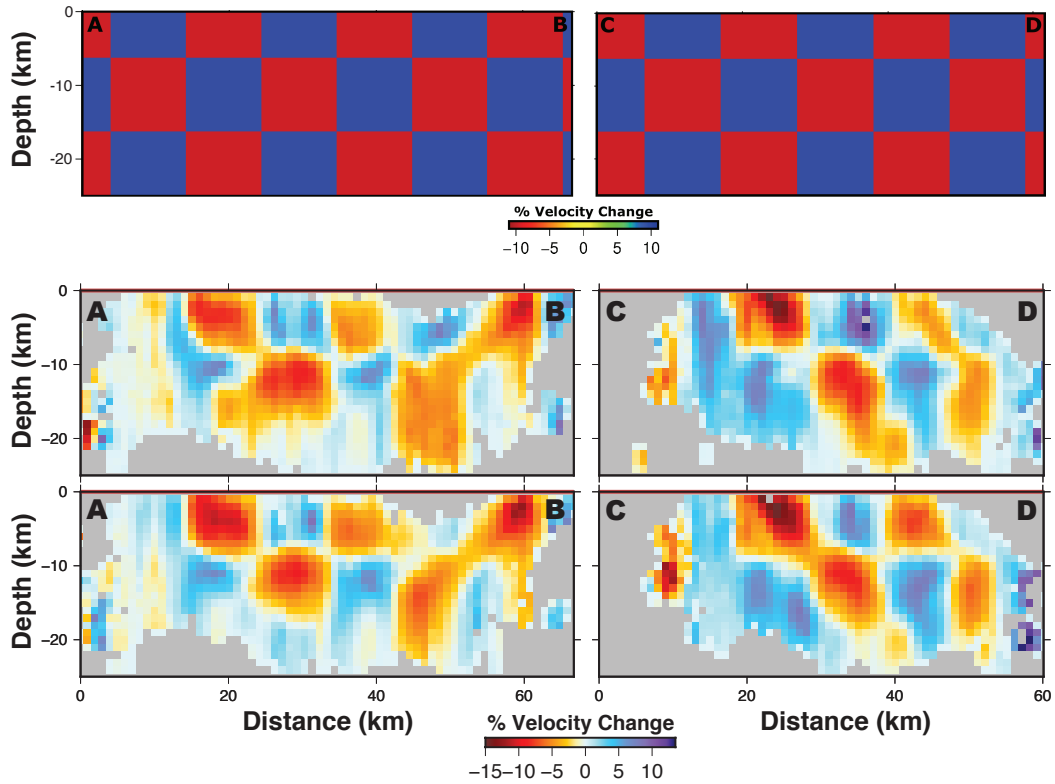


Figure 4. Vertical cross-sections of the checkerboard resolution test results as shown in Fig. 3. The top panel shows the input model of alternating blocks with $\pm 10\%$ velocity perturbations. The middle and bottom panels are the recovered checkerboard for P-waves and S-waves variations respectively. Profiles AB and CD are indicated in Fig. 3.

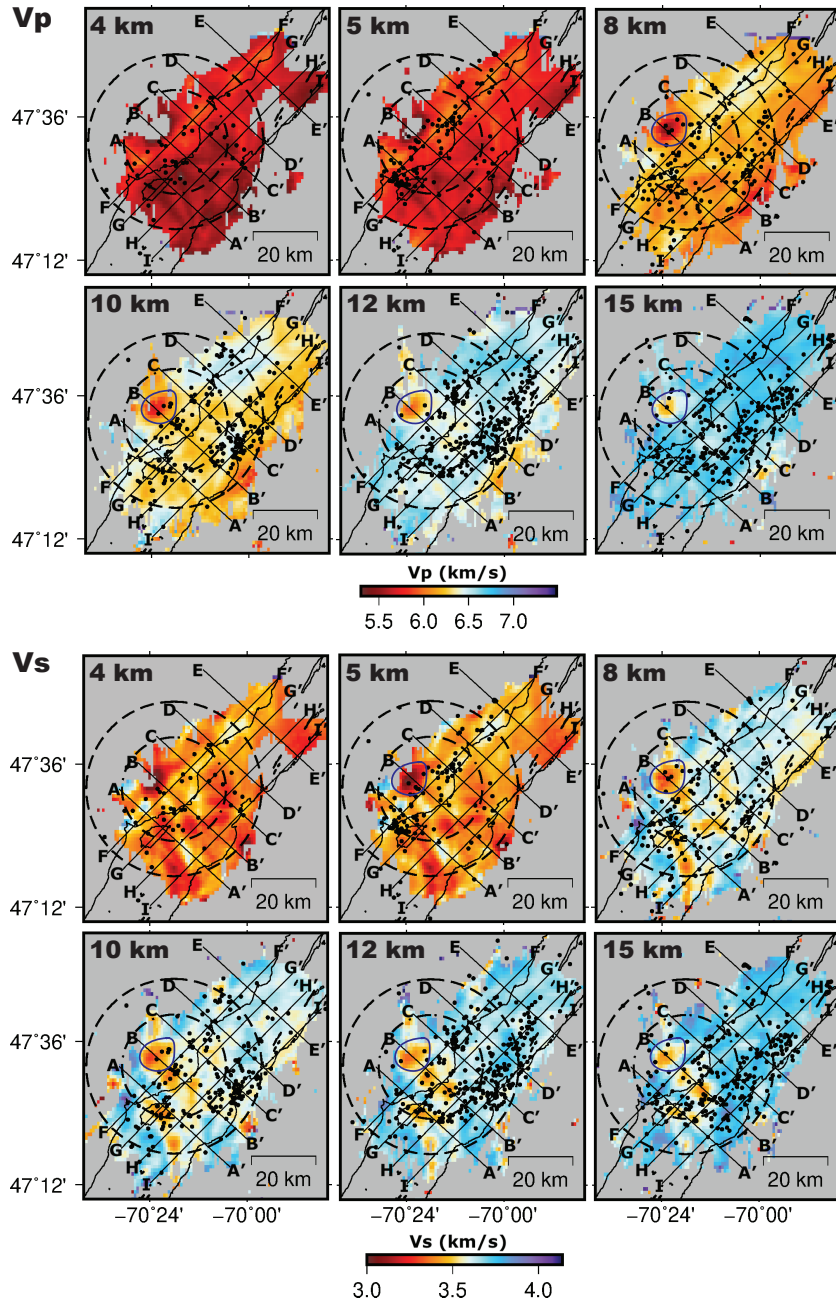


Figure 5. Depth slices of the absolute P- and S-wave velocities across the CSZ. The depth of each slice is indicated in each sub-figure. Black circles represent earthquakes located within 1 km of each depth slice. Black lines AA'-II' represent locations of profile lines in Fig. 4. Scale bars show range of V_p and V_s . Blue circled region highlights a lower velocity feature NW of the central uplift of the impact structure.

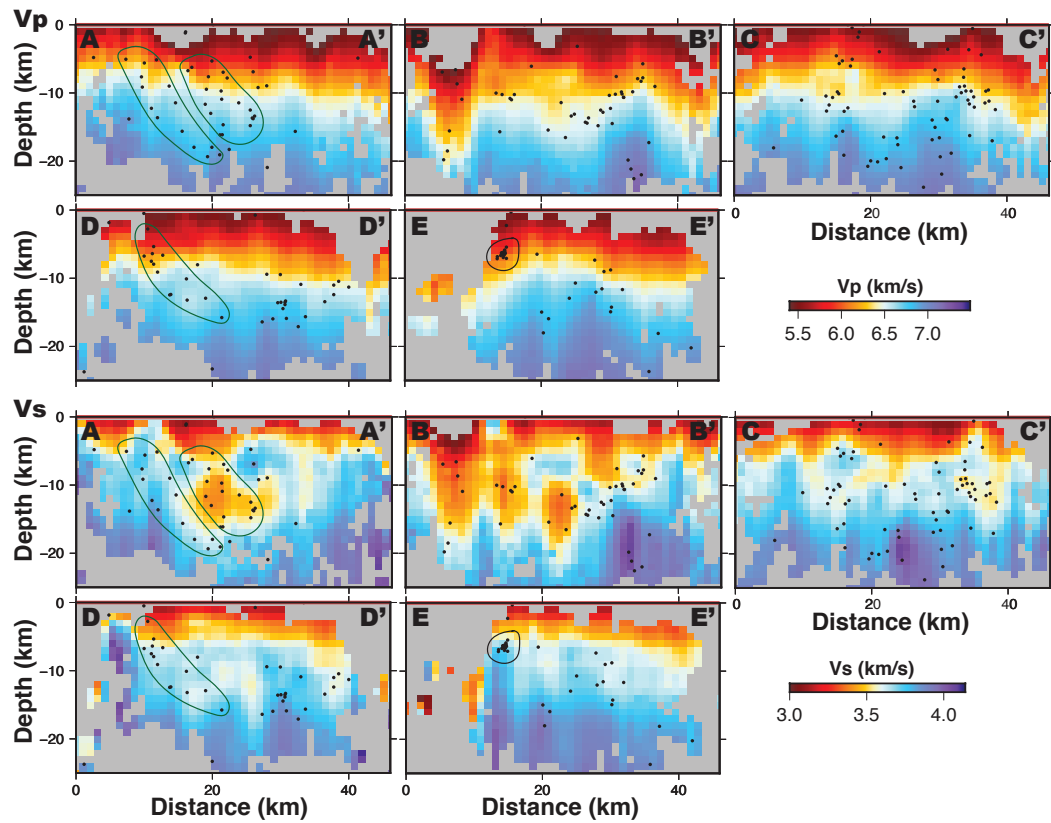


Figure 6. Vertical cross sections of profiles AA'-EE' for V_p (rows 1 & 2), and V_s (rows 3 & 4). Profile lines are shown in Fig. 5. Black circle highlights an earthquake cluster in the upper crust NE of the impact structure. Green ovals highlight seismicity along the Iapetan normal faults.

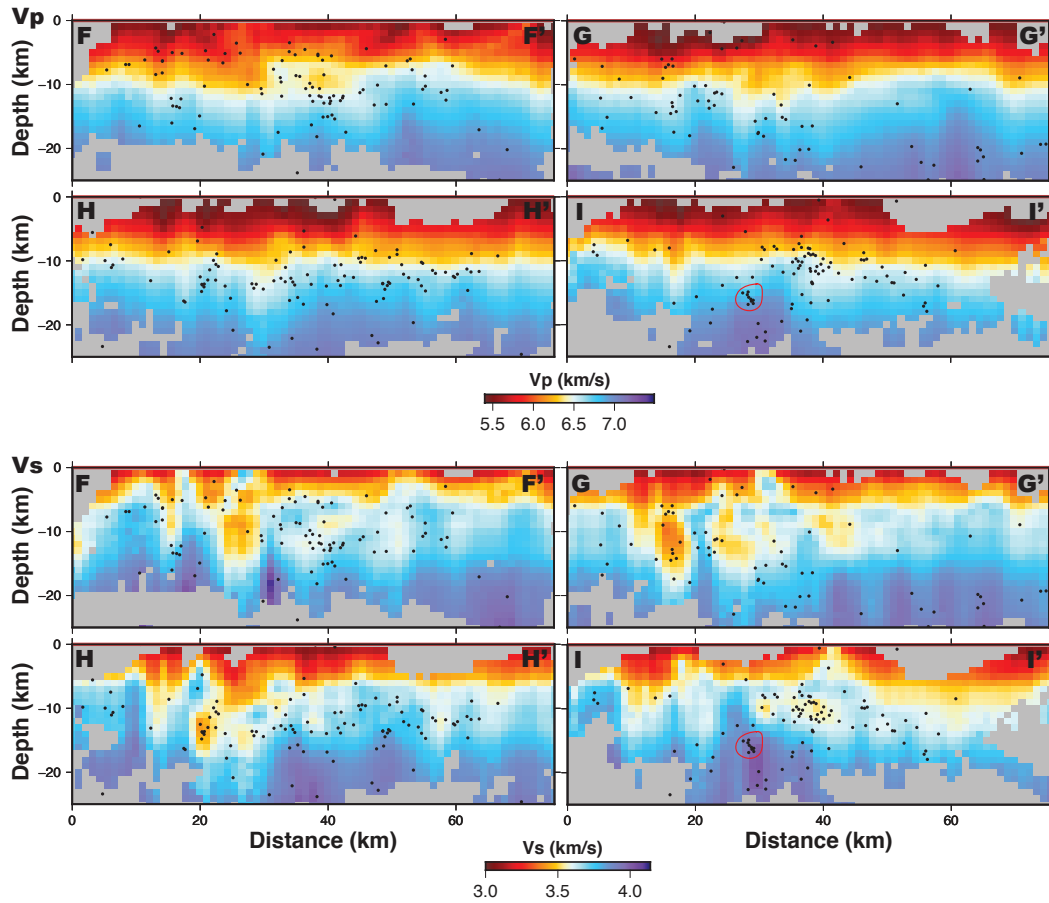


Figure 7. Vertical cross sections of profiles FF'-II' for V_p (rows 1 & 2), and V_s (rows 3 & 4). Profiles lines are shown in Fig. 5. Red circle highlights an earthquake cluster in the middle crust within the impact structure near the south shore of St. Lawrence River.

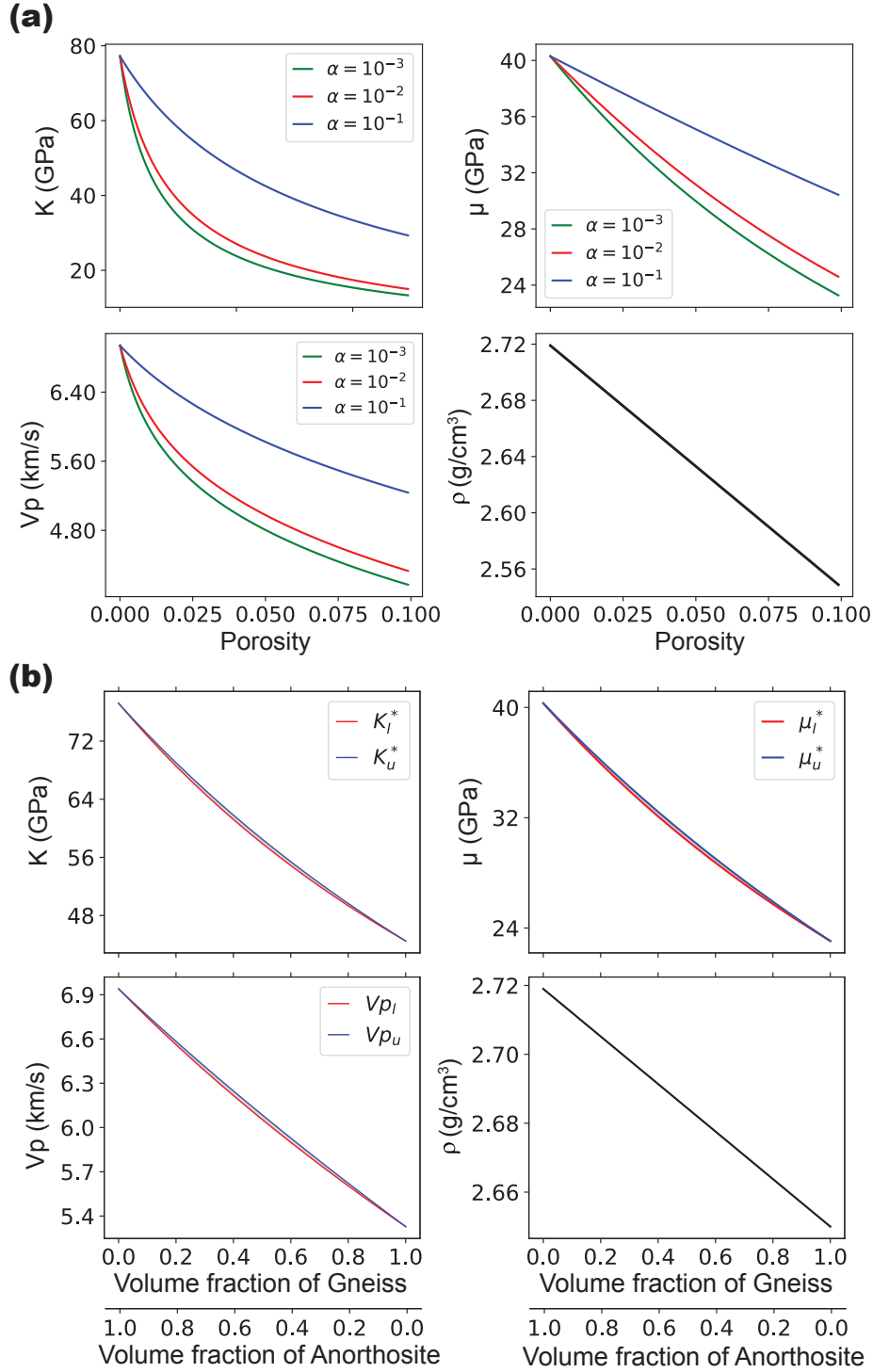


Figure 8. (a) Effective media analysis for a two-phase (anorthosite and water) media using the Kuster and Toksöz (1974) theoretical formulation. K , μ , ρ , and α represent bulk modulus, shear modulus and density of the effective medium, and crack aspect ratio. (b) Effective media analysis of a two-phase (anorthosite and gneiss) media derived with the theoretical relationship of Hashin and Shtrikman (1963). K_l^* , K_u^* , μ_l^* , μ_u^* , V_{pl} , V_{pu} represent the lower and upper bounds of bulk modulus, shear modulus and P-wave velocity of the effective medium. The proximity of the lower and upper bounds reflects the relative stiffness of the constitutive rocks.

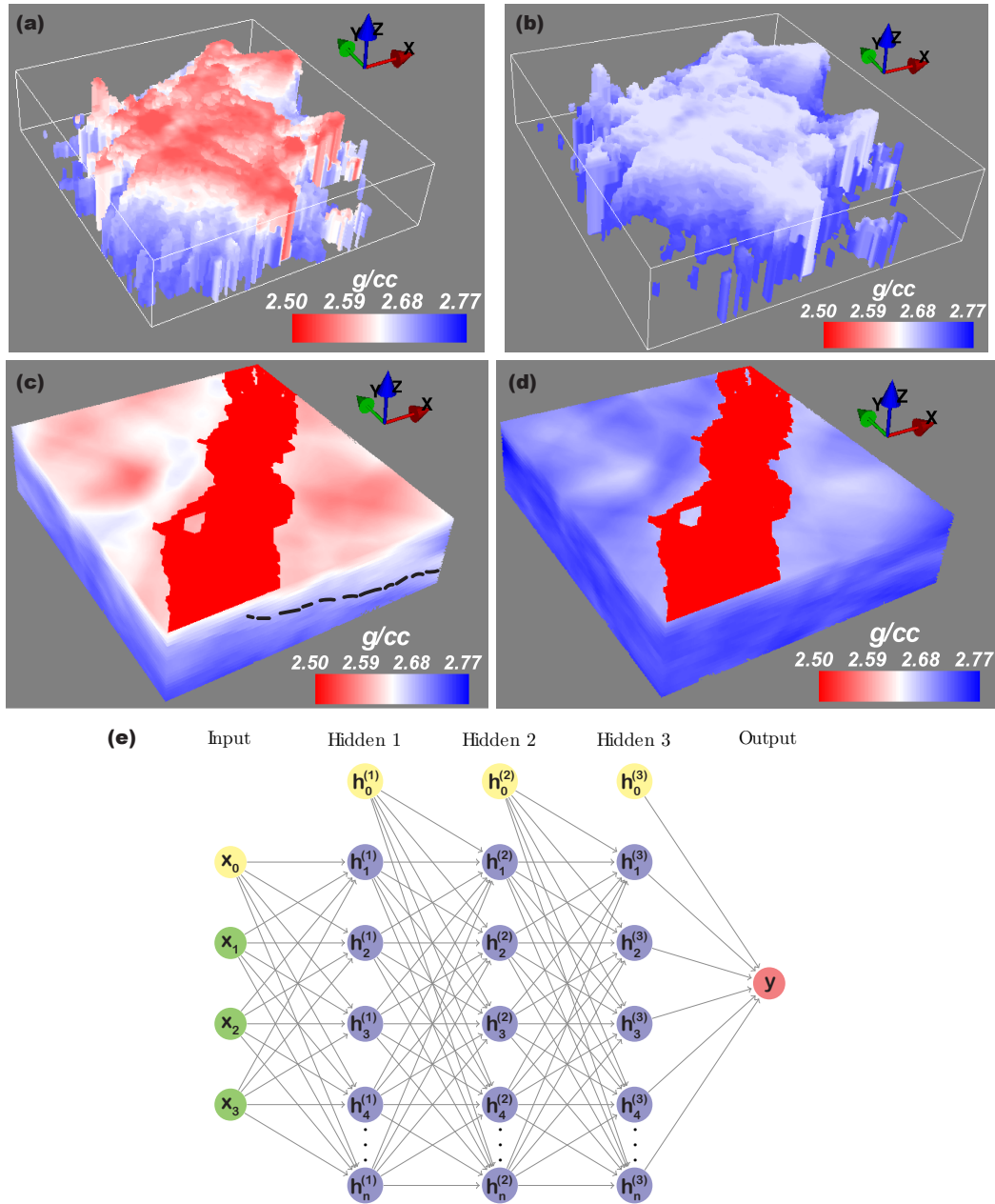


Figure 9. (a) & (b) Sparse 3D density model derived from effective media analysis with the Kuster and Toksöz (1974) and Hashin and Shtrikman (1963) theoretical formulations respectively. The sparse 3D density models are used as input for the neural network Multi-Layer Perceptron regression. (c) & (d) Full 3D density models determined from the regression analysis of (a) & (b) respectively. (e) The neural network with 3 hidden layers of 100 neurons each used for the Multi-Layer Perceptron regression. Dashed-black line in (c) could be the contact between Grenville Province and Appalachian rocks.

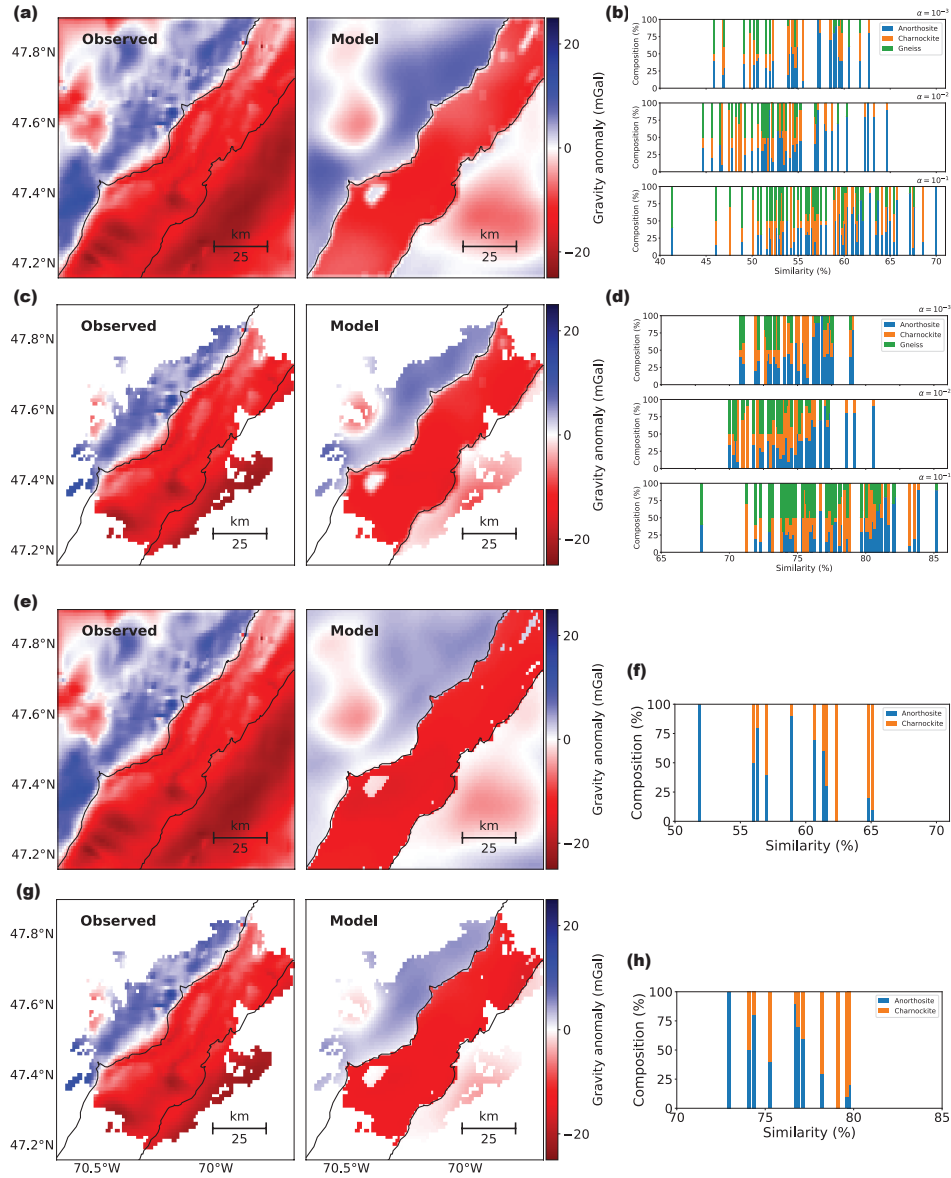


Figure 10. (a) & (b) Observed and best predicted residual gravity anomalies for the entire study area and respective similarity values for the intense fracturing scenario. (c) & (d) Observed and predicted residual gravity anomalies for the area with dense ray coverage (Fig. 2), and respective similarity values for the intense fracturing scenario. (b) & (d) show similarity of residual gravity anomaly predicted with the 165 3D density models to the observed Bouguer residual anomaly. (e) & (f) Observed and best predicted residual gravity anomalies for the entire study area, and respective similarity values for the compositional variation scenario. (g) & (h) Observed and best predicted residual gravity anomaly for the area with dense ray coverage, and respective similarity values for the compositional variation scenario. The predicted residual gravity anomaly was calculated with the same density model as in (e). (f) & (g) show similarity of residual gravity anomaly predicted with the 11 3D density models to the observed Bouguer anomaly.